Review article

Athanasia Kostopoulou*, Konstantinos Brintakis, Nektarios K. Nasikas and Emmanuel Stratakis*

Perovskite nanocrystals for energy conversion and storage

https://doi.org/10.1515/nanoph-2019-0119
Received April 20, 2019; revised June 18, 2019; accepted June 19, 2019

Abstract: The high demand for energy consumption in everyday life, and fears of climate change are driving the scientific community to explore prospective materials for efficient energy conversion and storage. Perovskites, a prominent category of materials, including metal halides and perovskite oxides have a significant role as energy materials, and can effectively replace conventional materials. The simultaneous need for new energy materials together with the increased interest for making new devices, and exploring new physics, thrust the research to control the structuring of the perovskite materials at the nanoscale. Nanostructuring of the perovskites offers unique features such as a large surface area, extensive porous structures, controlled transport and charge-carrier mobility, strong absorption and photoluminescence, and confinement effects. These features together with the unique tunability in their composition, shape, and functionalities make perovskite nanocrystals efficient for energy-related applications such as photovoltaics, catalysts, thermoelectrics, batteries, supercapacitor and hydrogen storage systems. The synthesis procedures of perovskite nanostructures in different morphologies is summarized and the energy-related properties and applications are extensively discussed in this paper.

Keywords: perovskite nanocrystals; energy conversion devices; energy storage devices; thermoelectrics.

***Corresponding authors: Athanasia Kostopoulou,** Institute of Electronic Structure and Laser (IESL), Foundation for Research and Technology Hellas (FORTH), P.O. Box 1385, Heraklion 70013, Crete, Greece, e-mail: akosto@iesl.forth.gr. https://orcid.org/0000-0002-7231-9876; and **Emmanuel Stratakis,** Institute of Electronic Structure and Laser (IESL), Foundation for Research and Technology Hellas (FORTH), P.O. Box 1385, Heraklion 70013, Crete, Greece; and University of Crete, Department of Physics, 710 03 Heraklion, Crete, Greece, e-mail: stratak@iesl.forth.gr. https://orcid.org/0000-0002-1908-8618
Konstantinos Brintakis: Institute of Electronic Structure and Laser (IESL), Foundation for Research and Technology Hellas (FORTH), P.O. Box 1385, Heraklion 70013, Crete, Greece
Nektarios K. Nasikas: Hellenic Foundation for Research and Innovation (HFRI), 127 Vass. Sofias Ave., 11521, Athens, Greece

1 Introduction

The high demand for energy consumption in everyday life activities along with fears of the climate changes highlight the importance to develop efficient energy conversion and storage devices. Thus, sufficient energy conversion and storage together with low-cost energy materials are the most important requirements. In order to design such devices, it is crucial to study and understand the underlying principles and mechanisms of renewable energy conversion and storage. Each of these technologies has its own characteristics, requirements, and efficiency limits or constraints. Different mechanisms take place in each technology and this is the main reason for dealing them independently.

The design and engineering of novel materials with a suitable range of properties for the effective utilization for such applications is a basic requirement. The design of new energy-related materials is at the forefront of different sciences such as the material science, chemistry, physics, and engineering. It is important to reveal the relationship between the material structure and the device performance if we wish to propose new energy-related materials [1–3].

In the quest to find prospective energy materials for high performance energy devices, the perovskite compounds hold a prominent role due to their unique tunable properties [4–8]. Perovskites are a family of materials with the formula ABX_3 and have a similar structure to the prototype $CaTiO_3$ mineral. The cation "A" occupies the corner positions of the unit cell and the cation "B" is located at the center of the cell, while the anion "X" is on the unit

cell faces [9]. This family comprises oxides and halide perovskite material. Some representative oxides are the ferroelectric $BaTiO_3$ and $PbTiO_3$, the dielectric $(Ba,Sr)TiO_3$, the piezoelectric $Pb(Zr,Ti)O_3$, the electro-strictive $Pb(Mg,Nb)O_3$, the magneto-resistant $(La,Ca)MnO_3$, and the multiferroic $BiFeO_3$. In the case of metal-halide perovskites, M is a divalent metal from group 14 (Pb, Sn) or a rare earth element (Eu), and X is a halogen (X=F, Cl, Br, I, or a combination of them). According to the nature of the cation, the metal halides can be divided in two groups, the all-inorganic and the hybrid organic-inorganic metal halides. In the first category the cation A is a monovalent alkali metal (like Cs, K) while in the second it is a small organic cation (such as CH_3NH_3) [10, 11].

The exploitation of new synthesis methods for the fine control of the structural characteristics and improved stability is important in the design of perovskite energy-related materials. Furthermore, the progress on the synthesis strategies for nanoparticulate systems of high quality in terms of homogeneity and crystallinity, has led the research community to search whether these materials could replace conventional energy materials. Different morphologies and chemical structures have been introduced for both metal halide and perovskite oxide nanocrystals for such purposes [1, 12, 13].

Metal halide nanocrystals can be effectively used in energy conversion, due to their strong optical absorption, low non-radiative recombination rates, tunable band gaps, relatively high charge-carrier mobility, and long diffusion lengths coupled with solution processability [14]. These nanocrystals have been utilized as the absorbing material in perovskite solar cells [15, 16] or placed at the interface between the absorbing and the hole transport layer (HTL) in order to improve carrier transport and stability [17, 18]. They are also used as down-converters in silicon solar cells due to their excellent quantum-cutting properties giving efficiencies of 21.5% [19]. In contrast, perovskite oxide nanocrystals have been utilized as electron transport layers (ETLs) in perovskite solar cells, as these materials are characterized by high electron mobility, wide band-gap, and a well-aligned conduction band with the absorbing layer [20]. Furthermore, perovskite nanocrystals have been tested for catalytic carbon dioxide (CO_2) reduction in solar fuel cells. By mimicking the natural photosynthesis in green plants, artificial conversion of CO_2 into chemical fuels offers a promising approach to simultaneously mitigate the levels of greenhouse gas and produce renewable energy [21]. Artificial solar-driven CO_2 reduction results in the partial reduction of the carbon monoxide (CO), methane (CH_4), methanol (CH_3OH), etc., which are common chemical fuels. Single-phase metal halide nanocrystals have shown promising results in CO_2 reduction [22, 23], but enhanced performance when these are coupled with graphene oxide (GO) or palladium nanosheets [24, 25]. Besides, the perovskite materials are promising materials for thermoelectrics for the conversion of thermal energy to electricity [26, 27]. Compared to the traditional materials used for thermoelectric applications (metal chalcogenide materials like Bi_2Te_3 and PbTe), perovskite materials are less expensive and can be processed by low energy cost methods and can be used for flexible thermoelectric devices [27]. The fairly ionic, polar character with a large dielectric constant and the remarkable conduction band anisotropy of the metal halides convey robust thermopower and moderate room temperature electrical conductivity [28].

Perovskite nanocrystals have been utilized in energy storage in batteries or supercapacitors due to their excellent catalytic activity, electrical conductivity, and durability. Ion migration through perovskite lattices allows the use of such materials as electrodes for batteries. Electrochemical measurements of the nanoparticulate perovskite systems displayed superior catalytic activity for oxygen reduction, as well as a higher discharge plateau and specific capacity compared to the bulk materials of the same crystal structure [29]. Metal halide nanocrystal films have been formed for application as anodes, for stable Li-based batteries [30–32]. Furthermore, in the case of the perovskite oxides, the size and the morphology of the nanocrystals are two factors that affect their electrochemical performance. Factors such as the structural nanocrystal quality, the existence of defects in the lattice [33], the doping in of the A and/or B site of the perovskite lattice [34–37], the nanocrystal porosity [38–41], and the existence of synergetic effects in the bifunctional morphologies [42–46] play an important role in the final electrochemical behavior. In addition, in the case of supercapacitor storage, it was found that structuring perovskite oxides and forming nanocrystals lead to remarkably enhanced, specific capacitance, rate capability, and cycle stability compared to the corresponding bulk materials [47–49]. Finally, perovskite nanocrystals offer improved electrochemical performance, low cost production in hydrogen storage and energy sustainability for transportation, electricity generation, and heating. Perovskite oxide nanocrystals show a higher discharge capacity compared to the bulk counterpart of the same stoichiometry [50] and in some cases is comparable to that of common materials that have been used for hydrogen storage to date [51].

Several review articles have been published on the application of nanocrystals in energy conversion and storage in the last couple of years [52–57]. This review article seeks to summarize the colloidal methods of the perovskite nanocrystals both for metal halides and perovskite oxides but mainly focuses only on the applications of the nanoparticulate structures (Figure 1). This review is structured in three main sections: Section 2 deals with the synthesis strategies, morphology, and size control of the single-phase perovskite nanocrystals, Section 3 looks at perovskite nanocrystals for energy conversion, and Section 4 deals with perovskite nanocrystals for energy storage. In all these sections, we have summarized the literature for both metal halide and perovskite oxide nanocrystals and discuss the effect of structure, morphology, and size in the performance of these devices. This review article concludes with some open issues that require attention to succeed in designing efficient and low-cost devices.

2 Synthesis strategies, morphology, and size control of the single-phase perovskite nanocrystals

Different methods have been introduced for the successful synthesis of perovskite nanocrystals. Metal halides have been synthesized by template-assisted methods and colloidal-based reactions, while perovskite oxides are created by solid-state or molten-salt reactions and colloidal processes. Due to the limited use in energy application of the metal halide nanocrystals synthesized by template-assisted methods we will focus only on the colloidal methods. In the case of the oxides, despite the fact that the solid state and molten-salt syntheses are more convenient compared to the colloidal ones, the latter have the advantage of achieving a better control of the characteristics of nanocrystals. Here, we focus on the

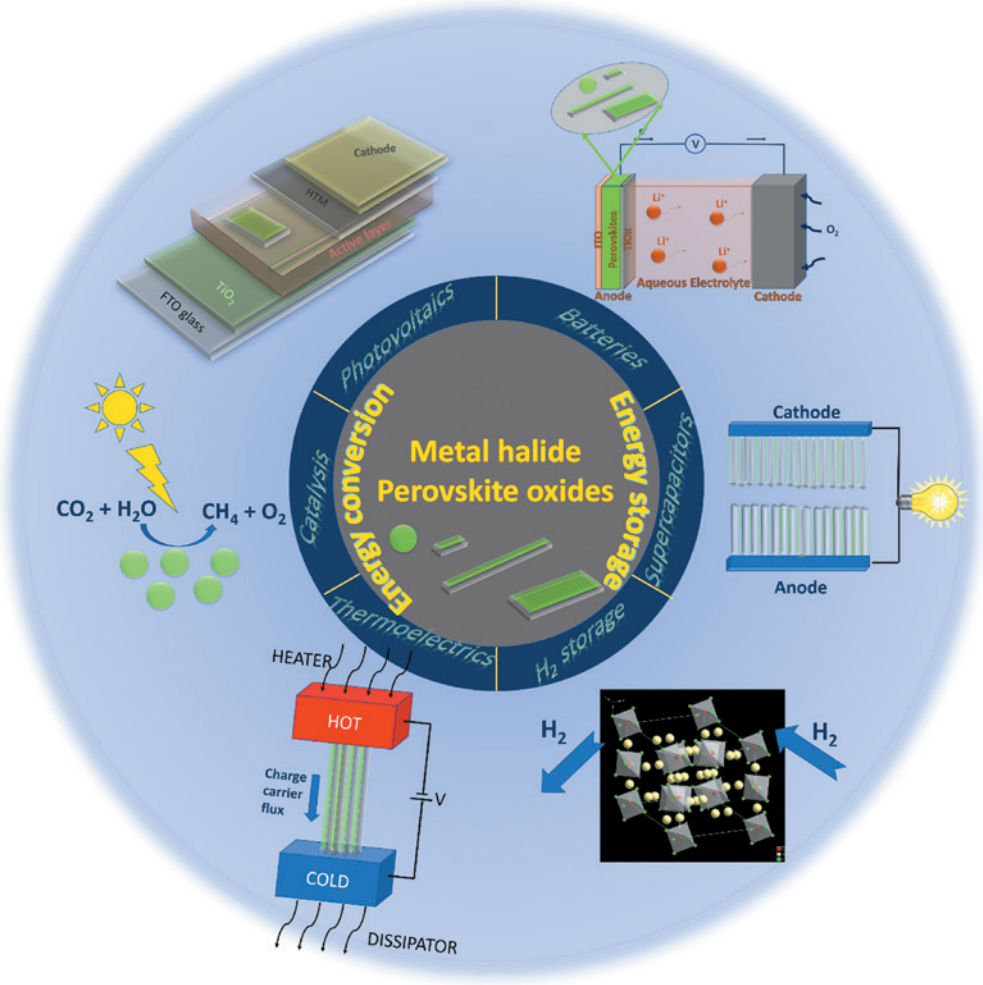

Figure 1: Applications of perovskite (metal halides and perovskite oxides) nanocrystals for energy conversion and storage.

colloidal methods that offer control on the morphology/structure and we think that they can be used to obtain energy devices of high performance with a reproducible and well-controlled manner despite whether they were used earlier or not.

Colloidal methods were used for the synthesis of both metal-halide and perovskite oxide nanocrystals of different morphology, isotropic or anisotropic one (Figure 2). In most cases, the metal halide nanocrystals were covered with organic molecules, usually acids and amines, while in the case of perovskite oxides, they are free of ligands (Table 1).

2.1 Colloidal synthesis for metal halide nanocrystals

Colloidal strategies at low or even at high temperature (>140°C) have been introduced for the morphological control of the metal halide nanocrystals through

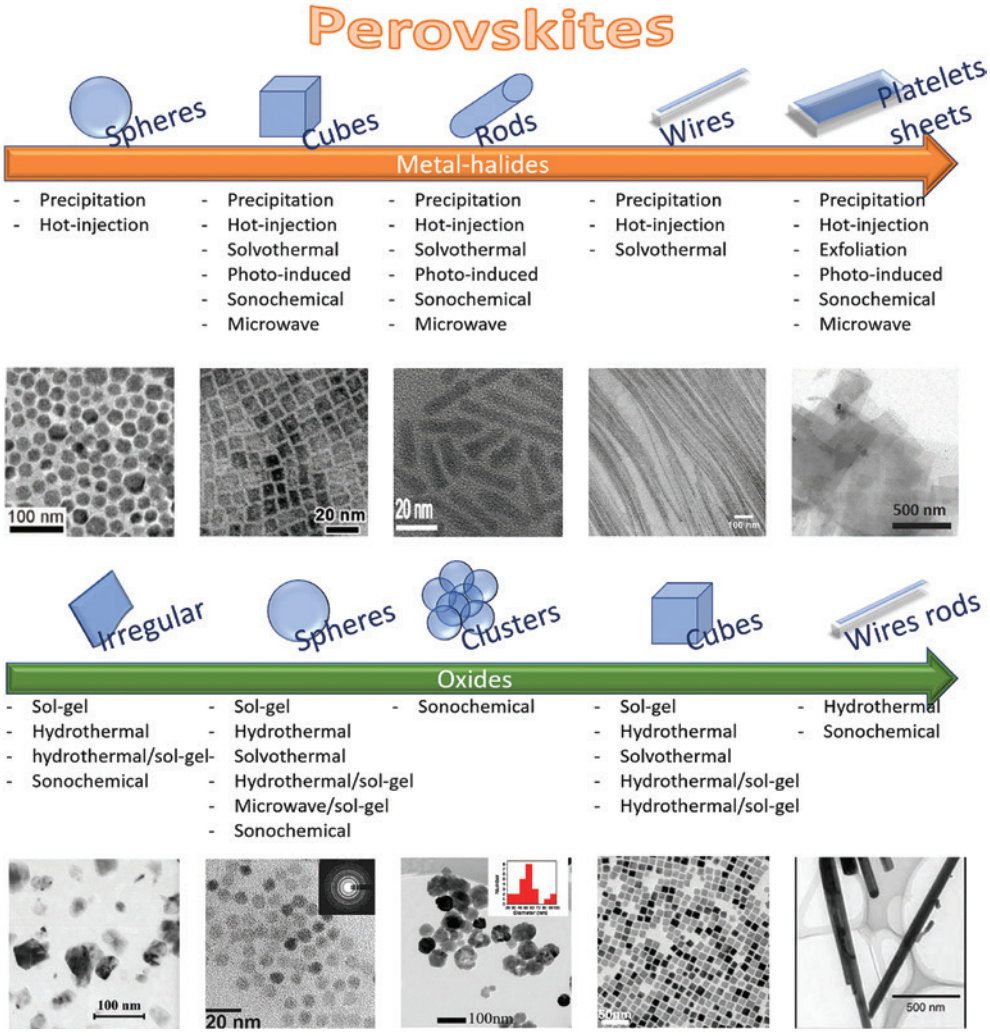

Figure 2: Summary of the solution-processed synthesis procedures of various perovskite nanocrystal morphologies. Metal halides: (a) Nanospheres synthesized by a hot method. (Reprinted with permission from [58] Copyright (2017), American Chemical Society.] (b) Nanocubes synthesized by ultrasound-irradiation. (Reproduced by permission of the Royal Society of Chemistry [59].) (c) Nanorods synthesized by solvothermal method. (Reprinted with permission from [60]. Copyright (2016), American Chemical Society.) (d) Nanowires synthesized by re-precipitation method. (Reproduced by permission of the Royal Society of Chemistry [61].) (e) Nanosheets synthesized by exfoliation. (Reproduced with permission from [62]. Copyright 2016, Wiley-VCH.) Perovskite oxides: (a) Irregular-shaped nanocrystals synthesized by sol-gel method. (Reproduced with permission from [63]. Copyright 2011, Elsevier.) (b) Spheres synthesized by the sol-gel method. (Reprinted with permission from [64]. Copyright (2001), American Chemical Society.) (c) Clusters synthesized by the sonochemical method. (Reproduced with permission from [65]. Copyright 2018, Elsevier.) (d) Cubes synthesized by solvothermal method. (Reproduced from [66] with permission from the Royal Society of Chemistry.) (e) Rods synthesized by hydrothermal methods. (Reproduced with permission from [67], Copyright 2005, Wiley-VCH.)

Table 1: Synthesis strategies summary for the perovskite nanocrystals in liquid form.

Phase	Method	Nanocrystal Morphology	Ligand/surfactant	Reaction temperature (°C)	References
Lead-halides	Precipitation-based methods	Quantum dots, spheres, cubes platelets, sheets, rods, wires, hexagons	Acids, amines	30 (only a few >30)	[32, 61, 68–82]
	Hot-injection methods	Spheres, cubes, rods, wires, platelets, sheets	Acids, amines, trioctylphosphine	Most of them >140 (only a few <140°C)	[58, 83–103]
	Solvothermal	Cubes, wires	Acids, amines	140–200	[104]
	Photo-induced	Cubes, irregular-shaped	No ligands	30	[105, 106]
	Sonochemical	Cubes, platelets	Amines	30	[59, 107]
	Exfoliation	Platelets	Amines	30	[62]
	Microwave-assisted	Cubes, platelets, rods	TOPO, acids, amines	30, 80–160	[108, 109]
Lead-free halides	Precipitation based methods	Spheres	Amines, phosphine, thiol	30	[110–112]
	Hot-injection method	Cubes, spheres	Acids, amines, no ligands	80–220	[113–115]
	Solvothermal	Rods	Acids, amines	180	[60]
	Hydrothermal	Spheres	Amines	180	[116]
Perovskite oxides	Sol-gel	Irregular-shapes, spheres, polyhedral, cubes, honey-comb-like	Free of ligands (in few acids)	400–1400 (only a few <400)	[63, 64, 117–135]
	Microwave sol-gel	Spheres	Free of ligands	1100	[136]
	Hydrothermal	Irregular, spheres, cubes, tubes, wires, complex shapes (dentrites, stars, sea-weed, torus, worm-like), hollow	Free of ligands, acids, amines, polyvinylpyrrolidone	80–400	[137–146], [67, 147–154]
	Hydrothermal sol-gel	Irregular, spheres, hollow, wires	Free of ligands	80–220	[36, 155–161]
	Hydrothermal-microwave	Cubes	Acids	200	[162]
	Solvothermal	Spheres, worm-like, cubes, hollow	Free of ligands, acids	150–200	[48, 66, 163–166]
	Solvothermal sol-gel	Spheres	Free of ligands	60–240	[167]
	Sonochemical	Irregular, spheres, clusters, rods, polygons	Free of ligands	30–80	[65, 168–172]

"top-down" or "bottom-up" approaches [12]. The first category comprises processes which start from molecules and ions and proceed with chemical reactions. In this type of reaction, the presence of capping ligands is important to control the size, morphology, and dispersity of the final nanocrystals. The second category includes the fragmentation of larger particles by an external stimulus such as irradiation or sonication in the presence of ligands or not.

Re-precipitation, hot-injection and solvothermal are the three main synthesis methods in the "bottom-up" approaches. The first one is a low-temperature process while the other two take place at high temperatures. All of them share common characteristics but have important differences [1]. For example, the re-precipitation methods are quick procedures, cost-effective, reproducible, they do not need complex apparatus, such as Schlenk line and inert gas flow, and are suitable for large-scale production. The hot-injection processes have a unique capability to finely control the shape and morphology of the nanocrystals, and also to produce complex structures with high homogeneity. This procedure is a time consuming procedure; it uses a Schlenk line coupled with a protective atmosphere and produces a small amount of the final product. Finally, the solvothermal process gives very good control of the nanocrystals by using a simple set-up, but the time duration of the reactions is a significant disadvantage of this procedure.

2.1.1 "Bottom-up" approaches

2.1.1.1 Room temperature re-precipitation methods

This solution-based process has been introduced to synthesize nanocrystals of different morphologies and chemical phases. The metal precursors are dissolved in a solvent usually in the presence of capping molecules. Then, this solution is added in a miscible co-solvent in which the solubility of the ions is low. Spontaneous crystallization and precipitation take place. This procedure has been proposed for both hybrid organic-inorganic or all inorganic metal halide nanocrystals and morphologies such as nanospheres [68–73], nanocubes [71, 72, 74–76], nanohexagons [32, 76], nanorods [70–72, 77], nanowires [61, 70, 72, 78], nanoplatelets [70–72, 79, 80, 173], and nanosheets [70, 81]. In addition, such methods were reported last years for the synthesis of lead-free nanocrystals with quantum dot morphology [110–112].

The first report on the synthesis of metal halide nanocrystals with this was in 2014 by the group of Pérez-Prieto for the production of spherical $CH_3NH_3PbBr_3$ nanocrystals with a 6 nm diameter [68]. The precursors in this reaction were CH_3NH_3Br and $PbBr_2$ while the capping molecules were the oleic acid together with long chain alkyl ammonium bromide. The dispersive solvent was octadecene while the co-solvent was acetone. Later, in 2015, in order to simplify this procedure, commercially available precursors and capping ligands (n-octylamine and oleic acid) were used [69]. This modified procedure resulted in similar morphologies but smaller in size (3 nm). N-dimethylformamide (DMF) was used as dissolving solvent and toluene as co-solvent.

By combining organic molecules of a long and a short chain, nanoplatelet morphologies were formed [79]. Their lateral dimensions can be tuned by regulating the surfactant ratio while by adjusting the oleic acid amount one can obtain very thin platelets down to one layer. By changing the ratio between octylamonium bromide and oleic acid, the particles can be changed from spheres to anisotropic nanorods [77]. The amines found mainly affect the size of the nanocrystals by controlling the kinetics of crystallization while the acids suppress the aggregation effects and contribute to the stability of the colloids [69]. Furthermore, the way of adding the precursor solution can affect the final size of the nanocrystals [70, 174]. A longer duration of the addition of the precursor results in larger particles through an Ostwald ripening mechanism [72] or anisotropic morphologies [70].

The type of solvent and co-solvent in which the precursors are dissolved can also affect the morphology of the final nanocrystals. Elongated particles have been synthesized by using acetonitrile or γ-butyrolactone as the dissolving solvent [70]. While when the cosolvent was the ethyl acetate, the obtained morphology is varied from dots to nanoplates to nanobars by increasing the reaction time while by using toluene the nanocrystals transform from nanocubes to nanorods to nanowires [72].

2.1.1.2 Room temperature sonochemical methods

Metal halide nanocrystals have been synthesized via ultrasonication techniques. The solution of the reactants together with the organic ligands are positioned in a high density probe-type ultrasonicator in order to fabricate cubic or platelet-like crystals [59, 107].

2.1.1.3 Hot-injection methods

This synthesis procedure is utilized for both lead-containing or lead-free metal halide nanocrystals (Table 1). This process includes the injection of a precursor solution in a hot liquid of the surfactants. A high-boiling point solvent is needed for these reactions. When the hot solution is injected, an instantaneous formation of nuclei takes

place. The nuclei grow slowly, due to the considerable amount of precursors, by increasing the temperature and the surfactant molecules coordinate on the surface of the nanocrystals. The relatively high temperatures of the reactions allow the annealing of the nanocrystals and the formation of well-crystallined and defect-free nanocrystals capped with the organic molecules. This method gives nanocrystals of small size and narrow size distribution. The size and the morphology found can be regulated by three crucial parameters during the synthesis: (i) the injection temperature of the precursor solution into the solution of the surfactants, (ii) the time of the reaction and (iii) the ratio of the precursors to the surfactants and the polarity of the reaction medium.

The first synthesis of metal halide nanocrystals using a hot-injection approach was reported by Kovalenko's group for cubic-shaped $CsPbBr_3$ nanocrystals of 4–15 nm edge length [83]. The reaction temperature is the main parameter that controls the size of the nanocubes in this case. Then, various morphologies such as nanospheres [58, 84–86, 113], nanocubes [83, 84, 87–93, 113], nanorods [60, 93], nanowires [94–98], nanoplatelets [85, 91–93, 99, 100] and nanosheets [98–101] have been synthesized. This wet chemistry method is also capable for fabricating more complex structures because the nucleation and the growth stages can easily be separated and controlled independently, that is not possible with the re-precipitation methods.

The role of the reaction medium polarity to the final morphology of the formed nanocrystals was described by the Zhang's group [84]. When the polarity of the solvent is high (diethylene glycol dibutyl ether and tetraethylene glycol dibutyl ether), spherical nanocrystals of 3–4 nm diameter are obtained. Cubes of 10 nm have been formed in a solvent with lower polarity (ethylene glycol dibutyl ether) with all the other parameters kept constant. The lateral dimensions of the nanocrystals can be tuned by lowering the temperature down to 90–130°C [91–93, 99–101]. The thickness of these large structures can be controlled by the reaction temperature as well as the type of ligands which are used for their capping [91]. Elongated nanocrystals have been synthesized at higher temperatures (150–250°C) but with longer reaction times [94, 96, 97].

2.1.1.4 High temperature solvothermal methods

In this method, the precursors and the surfactants are dissolved in a high boiling point solvent and closed in a sealed reaction container (stainless steel autoclave). The temperature is increased above the boiling point of the solvent and maintained at this temperature for a desired period. This method has been used for III–IV semiconductors and recently also for perovskite nanocrystals. This type of synthesis is based on the same starting materials with the previous methods, but it is capable for large-scale production. The first synthesis of perovskite nanocrystals with this approach was reported in 2016 from Chen's group [60]. Lead-free tin halide nanorods were fabricated at a temperature of 180°C and reaction time of 6 h.

Such a method has also been utilized for the synthesis of all-inorganic nanocubes or nanowires at 160°C [104]. Without pre-dissolving of the precursors, the final morphology of the nanocrystals are cubes while when this step takes place the final results are nanowires due to the higher concentration of the precursors.

2.1.2 "Top-down" approaches

2.1.2.1 Room temperature exfoliation

Hybrid organic-inorganic metal halide nanoplatelets of varied thickness have been obtained through the exfoliation of bulkier particles/microcrystals synthesized previously via a solid-state reaction [62]. These microcrystals are dispersed in an organic solvent together with a capping ligand and this solution is placed on a tip sonication. Different steps of centrifugation lead to nanoplatelets of different thickness. This method can be used for very thin nanoplatelets down to that of single unit cell.

2.1.2.2 Room temperature photo-induced methods

Two reports exist about the use a laser-induced procedure for the synthesis of metal halide nanocrystals. In the first, the nanocrystals were obtained through a photo-fragmentation process from larger particles. Bulk crystals grown by inverse temperature crystallization grinded into smaller structures in an organic solvent [105]. Ten minutes of irradiation with 532 nm laser pulses (9 ns, 10 Hz, 0.8 J/cm^2) of a Nd-YAG laser was enough to obtain cubic nanocrystals of around 60 nm. The ligand protects from the continuous growth of the crystals. In the second, a laser-ablation of metal-halide bulk material was used to obtain nanocrystals of the same phase [106]. This material was placed in the bottom of a vial containing an organic solvent together with an organic capping ligand. Nanocrystals of around 30–70 nm were formed after irradiation for 70 min with a 532 nm laser.

2.1.2.3 High temperature and room temperature microwave-assisted methods

In the first process, all the reactants are mixed together in a microwave tube in air atmosphere in contrast to the

protective atmosphere of the hot-injection method [108]. Then the tube is placed in a microwave reactor and the temperature is increased gradually. The shape of the all-inorganic metal halide nanocrystals synthesized by this method at high temperature are small cubes while they are plate-like for lower temperatures. Ultra-thin nanowires are obtained when the precursors are pre-dissolved before increasing the temperature. The role of the trioctylphosphine oxide (TOPO) ligand is important in this reaction, it favors the dissolution of the precursors and thus helps to obtain high-quality nanocrystals.

Besides, this reaction can take place at room temperature [109]. In this case the ligand is bis(2,4,4-trimethylpentyl) phosphinic acid (TMPPA) instead of oleic acid and the precursor is cesium acetate instead of cesium carbonate, and cubic nanocrystals of 19 nm in size are formed. The type of the precursor plays an important role in the luminescence properties. The luminescence is higher when CsOAc is used as the precursor compared to that of using Cs_2CO_3.

2.2 Colloidal synthesis for perovskite oxide nanocrystals

Solid-state reaction or molten-salt methods have been extensively used for the synthesis of perovskite oxide nanocrystals. These two processes are easy and use simple equipment. The nanocrystals synthesized by such methods are well-crystallined but they have irregular shapes and wide size distribution. The solid-state reactions take place at high temperatures while the molten-salt method at moderate ones (600–800°C) due to the existence of the inorganic molten salt which serves as a medium to enhance the reaction rate and reduce the temperature of the reactant oxides [13]. The solid-state process has been used to synthesize simple shapes such as irregular-shaped or spherical nanoparticles [175–177], and only a few reports exist for nanocubes or nanowires [178]. The starting materials are mixed together, a milling process is followed and then calcination at high temperature. In contrast, the molten-salt method has been proposed for various structures including irregular shapes [179–184], morphologies of high-aspect ratio [185–188] and platelets [189]. In order to have a better control over the morphology than the previous methods, bottom-up solution-processed approaches have been realized including sol-gel, hydrothermal, solvothermal, sonochemical, or microwave-assisted reactions (Table 1, Figure 2). Lower temperatures and in some cases organic ligands are utilized in such approaches.

2.2.1 Sol-gel methods

In these methods, a sol is formed when metal alkoxide, metal-organic, or metal-inorganic salt precursors are dissolved in an appropriate solvent, it is then dried and sintered at high temperatures. The morphologies obtained by this approach are irregular-shaped [63, 117–126, 136, 190] and spherical [64, 127–130]. Only a few reports exist about this method for different structures such as cubic [64, 131] or honeycomb-like [132] structures. Reaction parameters which play important role on the morphology and the size of the synthesized nanocrystals are the temperature, time of the reaction, and heating rate [133], as well as the usage or not of an organic ligand [64, 119, 123]. In order to save energy and to be cost effective, a sol-gel approach combined with a microwave-assisted sintering has been proposed for perovskite oxide nanocrystals [136].

2.2.2 Hydrothermal methods

An aqueous suspension of insoluble salts is positioned in an autoclave and the temperature is increased. Precipitation from the solution of the crystalline material occurs at temperatures between the boiling point and the critical point of water. Various and more complex morphologies including randomly-shaped [137–139], spheres [140–144], cubes [141, 145–147, 163], nanowires [67], nanotubes [148], as well as more complex dendrite [149] or star-like [150] structures have been synthesized by this method compared to the simple structures synthesized by the sol-gel method. The combination of hydrothermal with sol-gel method has been used for the synthesis of rounded/randomly shaped [36, 155–159], hollow [160], or elongated [161] nanocrystals. A microwave-hydrothermal process has also been utilized for the synthesis of cubic perovskite oxide nanocrystals [162].

2.2.3 Solvothermal methods

The solvothermal method is a general procedure for perovskite oxide nanocrystals that are free of ligands. The first synthesis was performed by Antonietti's group for the synthesis of irregular shaped $BaTiO_3$, $BaZrO_3$, and $LiNbO_3$ nanocrystals [164]. Lithium or barium metal was dissolved in benzyl alcohol at slightly elevated temperature. Then a metal alkoxide was added to this solution, placed in an autoclave and heated in a furnace at temperatures between 200 and 220°C for more than 2 days. Benzyl alcohol has been proved to be a versatile solvent and reactant for controlled crystallization and stabilization of oxidic

nanocrystals. The solvent polarity is crucial for the morphology control of the nanocrystals. The nanocrystals can be spheres or cubes by tuning this parameter [66]. The size can also be tuned by changing the precursors concentration and the temperature of the reaction. This method has been used for the efficaciously synthesis of spherical [66, 164–166], cubic [66, 166] or even hollow [48] morphologies.

2.2.4 Sonochemical methods

These processes take place at room temperature, where all the reactants are dissolved in a solvent under ultra-sound irradiation. With this method, irregular-shaped [65, 168], spherical [169, 170], rods [171], and polygons [172] are fabricated. All of these nanocrystals are free of ligands.

2.3 Perovskite nanocrystals for energy conversion

2.3.1 Perovskite nanocrystals in solar cells

2.3.1.1 Metal halide nanocrystals in perovskite solar cells

The metal halide nanocrystals have been used in perovskite solar cells by forming the active layer and/or placing them at the interface.

(i) Perovskite nanocrystals as active layer
Metal halide nanocrystals of various morphologies and chemical phases have been used as absorber material in perovskite solar cells. Hybrid organic-inorganic lead halides of spheres [191, 192], nanosheets [193] and nanowires [103, 194] have been used for active layer with the nanowires to show the higher efficiency to date (18.7%) [103]. Although, all-inorganic lead halides nanocrystals with spherical [16, 195–198], cubic [15, 199, 200] and elongated [201] morphologies have been used reaching an efficiency of 13.43% [202]. The Nanocrystals which showed this efficiency have a cubic morphology and they are capped with oleic acid [202].

The first hybrid organic-inorganic nanocrystal-based solar cell was reported by Park's group in 2011 [191]. In the case of the hybrid organic-inorganic solar cells, the efficiency was increased as the perovskite nanocrystal morphology changes from the spheres (2.4–6.54%) [191, 192] to nanosheets (10%) [193] and nanowires (14.71–18.7%) [103, 194]. The use of nanowires in the photoactive layer is an effective way for enhancing light trapping and improving charge transport efficiency. For this reason, the charge separation and conductivity were higher in the case of the nanowires compared to the bulk film [103, 196]. Very recently nanowires synthesized from the same chemical phase synthesized by a two-step spin coating process have reached the value of the 16.8% (Figure 3) [103]. Partially developed perovskite nanowires in the photoactive layer contribute more to photocurrent generation than in compact films (Figure 3E, F). These nanowires' solar cell efficiency improved by using a $PC_{60}PB$ additive and as a result raised the power conversion efficiency (PCE) to 18.7%.

Later in 2016, all-inorganic metal halide nanocrystals were used in perovskite solar cells instead of hybrid organic-inorganic materials to improve their stability [15, 16]. α-$CsPbI_3$ nanocubes of 9 nm edge length were introduced and the perovskite solar cells showed the high efficiency of 10.77%. This high efficiency has been attributed to the stable cubic phase (and not to the orthorhombic unstable phase) in which the nanocubes are crystalline [15]. It is known that the $CsPbI_3$ chemical phase which exhibits the smallest band gap is not structurally stable in the bulk form. Direct deposition of the $CsPbI_3$ nanocubes by spin casting, followed by stabilization of the perovskite structure via post deposition chemical treatment or annealing, contributed positively to the high quality of the active layer. The efficiency can be improved more and reach a value of 13.43% by tuning the surface chemistry via an A-site cation halide salt (AX) treatment (Figure 4A) [202]. The AX treatment provides a method for tuning the coupling among the nanocubes and improving the charge transport. The mobility of the treated film doubles, enabling an increased photocurrent and improved efficiency. Furthermore, higher stability has been observed in similar nanocrystals capped with TOP synthesized using a hot-injection method and a PbI_2/GeI_2 dual iodine source [200]. These nanocubes showed a near unity photoluminescence (PL) quantum yield and improved chemical stability compared to the previous systems. The ensuing nanocubes solar cells deliver PCE of 12.15% and retain 85% of its peak performance after storage over 90 days.

In a different approach, all-inorganic metal halides have been introduced into the absorber $MAPbI_3$ layer to reduce charge recombination and improve the charge transfer [203]. This process was used to improve the quality of the absorber layer in terms of film structure, morphology, and crystallinity as the nanocrystals behave as nucleation centers in the growth of perovskite films. The high quality of the films leads to improved charge transport and

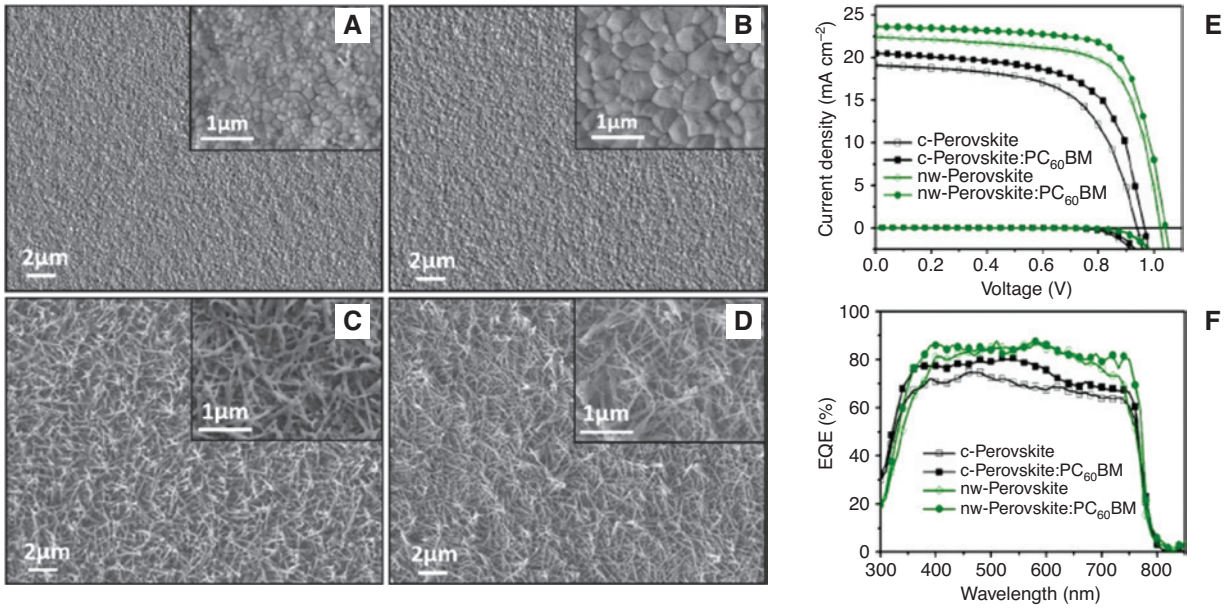

Figure 3: $CH_3NH_3PbI_3$ nanowires in perovskite solar cells.
Scanning electron microscopy (SEM) images of the c-perovskite (compact): (A), c-perovskite: $PC_{60}BM$ (B), perovskite nanowires (nw), (C), perovskite nanowires: $PC_{60}BM$ (D) films. J-V characteristics measured under sun and dark conditions (E), and EQE spectra for the highest-performing films (F). Reproduced with permission from [103]. Copyright 2018, Elsevier.

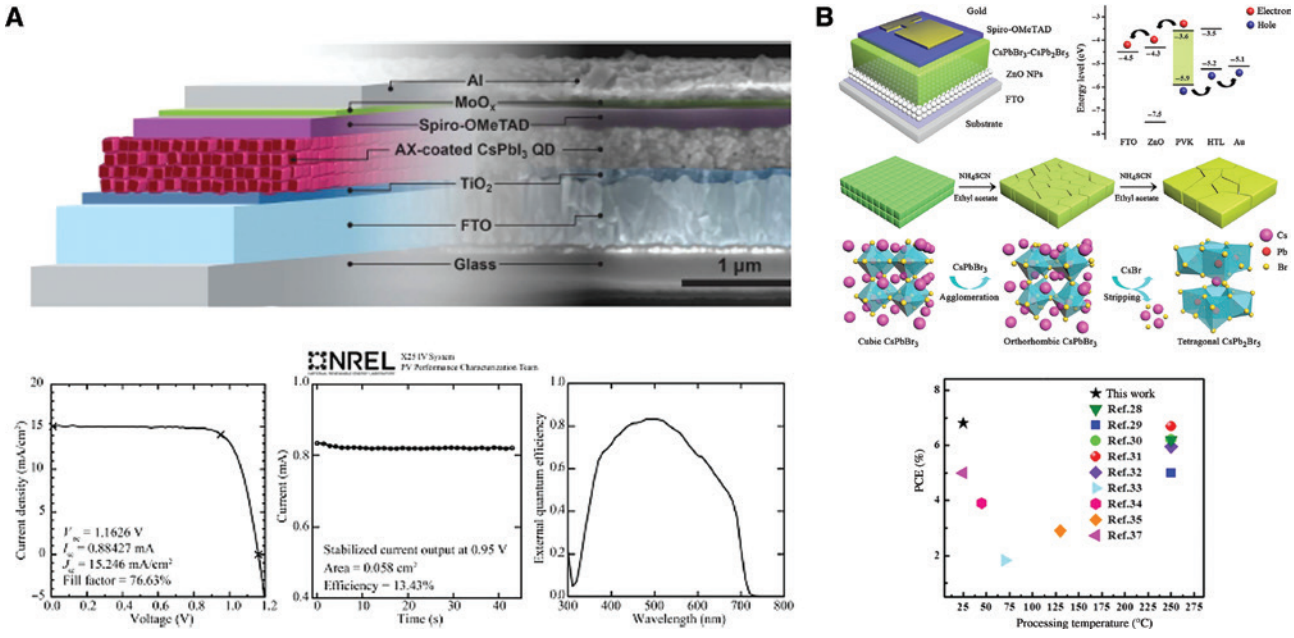

Figure 4: (A) Schematic representation of the AX-coated $CsPbI_3$ quantum dot sensitized solar cell, IV, and external quantum efficiency results. Reproduced with permission from [202]. Copyright 2017, AAAS. (B) Schematic structure of the device using $CsPbBr_3$-$CsPb_2Br_5$ composite as an absorbed layer, fabrication process and comparison with fabricated layers at higher temperatures in the literature. (Reprinted with permission from [196]. Copyright (2018), American Chemical Society).

solar cell PCE. At the same time, a protecting passivation layer of $Cs_{1-y}MA_yPbI_{3-x}Br_x$ is formed on the top of the perovskite absorber layer and this contributes to the final stability of the solar cell. A champion PCE of 20.46% is obtained from the perovskite solar cells based on high quality perovskite film.

Anion exchange at ambient conditions verified that this process could be an effective and simple

way to obtain mixed halide nanocrystals and showed really promising results in perovskite solar cells [198]. These perovskite solar cells displayed a photoconversion efficiency of 5.3% and open circuit up to 1.31 V. In addition, cation exchange approaches for tunable A-site alloys of cesium (Cs^+) and formamidium (FA^+) lead triiodide perovskite nanocrystals ($Cs_{1-x}FA_xPbI_3$) lead to quantum dot solar cells with high open circuit voltage (V_{OC}) with a lower loss than the thin-film perovskite devices of similar compositions [204]. These solar cells showed an efficiency of 10%.

Furthermore, $CsPbBr_3$ was developed and applied as "inks" to fabricate fully air-processed, electrical stable solar cells exhibiting a PCE exceeding 5%. This method provides a new pathway for single-step, large-scale fabrication of inorganic perovskite solar cells. Inks of $CsPbBr_3$ nanocrystals of 15–20 nm synthesized with a fast room temperature synthesis using short, low boiling point ligands and environmentally friendly solvents, have been proposed by Manna's group [16]. These inks can be used directly to fabricate films of high optoelectronic quality. An active layer of 550 nm prepared by nine sequential depositions, exhibited a PCE of 5.4% and a $V_{OC} = 1.5$ V.

The quality of the absorber layers of $CsPbBr_3$ can be improved further by treating them using an NH_4SCN ethyl acetate solution to quickly transform the $CsPbBr_3$ nanocrystals film into $CsPbBr_3$-$CsPb_2Br_5$ composite film (Figure 4B) [196]. The treated film is uniform and compact after a surface dissolution-recrystallization process, with large grain size and low defect density. The recorded PCE by using this composite was 6.81% in this case.

Finally, lead-free metal halide nanocrystals, free of toxic elements, were also introduced in perovskite solar cells. Tin-based metal halide nanocrystals have been synthesized in the form of nanospheres [205] or nanorods [60]. The efficiency of the devices using hybrid organic-inorganic tin halide nanospheres was 8.79% [205], while the efficiency of the devices including all inorganic nanorods can be ranged from 9.66 to 12.96% depending on the metal halide composition. The highest solar cell performance was recorded for the device using the phase $CsSnI_3$ [60]. These nanorods exhibit colloidal stability in air for more than 2 months and a decomposition temperature significantly higher than that of $MAPbI_3$. The photovoltaic parameters recorded for such devices were a short-circuit current density (J_{sc}) = 23.21 mA/cm^2, open-circuit voltage (V_{oc}) = 0.86 V, fill factor (FF) = 0.65, and PCE of 12.96%. In addition, recently reported all inorganic bismuth-based cesium halide nanocrystals in the form of nanosheets of 4.3 nm in thickness, synthesized by a dissolution-recrystallization process and were used for such applications [206]. The efficiency of this device was 3.2% but it is the highest reported to date in bi-based solar cells.

(ii) Perovskite nanocrystals at interfaces

Metal halide nanocrystals have been used at the interface between the perovskite absorbing layer and the HTL [17, 18]. The interface engineering is an effective way for obtaining high efficiency and improved stability in the perovskite solar cells through interfacial charge transfer control. A layer of hybrid organic-inorganic $FAPbX_3$ quantum dots is placed between the absorbing $MAPbI_3$ layer and the C_{60} HTL [17]. In this way, an increased short-circuit current and an improved solar cell efficiency by 43.7% were observed. Moreover, all inorganic α-$CsPbI_3$ quantum dots have been placed at the same position and the PCE increased from 15.17 to 18.56% in solar cells using $MAPbI_3$ as the absorbing material [18]. The charge-transfer efficiency at the interface of the perovskite/HTL is enhanced by $CsPbI_3$ quantum dots due to their intermediate valence band position between the perovskite and the HTL. In addition, the enhancement of the stability of perovskite solar cells can be attributed to the coating of the perovskite layer with the all inorganic $CsPbI_3$, which has a high moisture stability and results in long-term stability of the perovskite solar cells in the air.

In order to make stable the hybrid organic-inorganic quantum dots, they are covered with a shell of C18 [207]. These core-shell quantum dots – C18 were also used at the interface with the HTL. The efficiency of these solar cells reaches over 10%. The presence of long chain ligands bound to the quantum dots did not appear to damage hole extraction.

2.3.1.2 Metal halide nanocrystals in dichalcogenide quantum dot sensitized solar cells

All-inorganic metal halide nanocrystals have been employed as carrier blocking layers between the absorber layer of PbSe nanocrystals and the metal contact in dichalcogenide quantum dots sensitized solar cells [208]. The relatively large E_g (2.4 to 2.7 eV) of the $CsPbBr_3$ nanocrystals compared to that of PbSe nanocrystals (1.2 to 1.5 eV) was the crucial factor to use them as a blocking layer. On the one hand, these nanocrystals have been chosen for their good air-stability, their high photoluminescence quantum yield and their ability to be synthesized independently and on the other hand, the quality of the perovskite layer

seems not to be affected by the PbSe quantum dot layer. The PCE of this solar cell configuration is 7.2%. An open-circuit voltage (V_{OC}) of 482 mV, a current density (J_{SC}) of 23.9 mA/cm^2, and a fill factor (FF) of 62.4% under one-sun conditions were recorded.

In a different approach, the metal halides were utilized as a passivation layer on the surface of the dichalcogenide quantum dots (PbS) forming a core-shell structure [209–211]. A shell of hybrid organic-inorganic $MAPbI_3$ [209, 210] or all-inorganic $CsPbI_3$ [211] metal halide was introduced for quantum dot passivation. In the first case, the film of the core-shell nanocrystals was incorporated in a photovoltaic device with graded band structure and recorded a PCE of 8.95% for this solar cell [209]. Two years later, a funtionalized quantum dot HTL was introduced in such structures to block the back flow of the photogenerated electrons, leading to enhanced photocurrent and fill factor compared to undoped devices [210]. The ligand of the quantum dots was 1,2-ethanedithiol (EDT) and the solar cell performance reached the value of 9.5% due to the enhanced bending at HTL-absorber junction. The utilization of an all-inorganic shell around the PbS quantum dots led to a performance of 10.5% [211]. In this case the shell was epitaxially grown on the core surface. The improved passivation significantly diminished the sub-bandgap trap-state-assisted recombination, leading to improved charge collection and therefore higher photovoltaic performance.

2.3.1.3 Metal halide nanocrystals in dye-sensitized solar cells

Irregular-shaped, free of ligands, hybrid organic-inorganic perovskite nanocrystals were used to enhance the light absorption of dye-sensitized solar cells employing liquid electrolytes [212]. This incorporation resulted in a photovoltaic efficiency of 3.8% and photovoltage of 1.0 V. In this device, nanocrystalline particles of $CH_3NH_3PbX_3$ (X=Br, I) were deposited onto the TiO_2 surface by a self-organization process, starting with the coating of a precursor DMF-based solution. This $CH_3NH_3PbX_3$-deposited TiO_2 electrode was used as photoelectrode (anode) together with a Pt-coated FTO glass as counter electrode (cathode) and a 50 μm-thick separator layer. The gap between the electrodes was filled with an organic electrolyte solution containing lithium halide and halogen as a redox couple. A higher PCE was measured for the $CH_3NH_3PbI_3$ perovskite sensitizer (3.8%) among the different stoichiometries tested.

Furthermore, spherical amine-capped $CH_3NH_3PbI_3$ nanocrystals synthesized by a re-precipitation method have been introduced in quasi-solid-state sensitized solar cells with a configuration FTO/m-TiO_2/perovskite quantum dots/dye/long persistence phosphor/gel electrolyte/Pt/FTO [213]. The perovskite nanocrystals were employed as charge-transfer bridge between the TiO_2 and the N719 dye to extract photo-induced charges from a light-harvester. From the metal halides tested, the $CH_3NH_3PbBr_{1.5}I_{1.5}$ nanocrystals have been proved as the most preferred co-sensitizers for the efficiency enhancement due to their optimal energy level compared to that of a dye molecule, in which the photogenerated electrons from the dye molecule can transfer to nanocrystals and then to TiO_2. Furthermore, the long persistence phosphor (LPP) which has light-storing and light-emitting ability covered the m-TiO_2 layers aiming to harvest the longer wavelength light which permeated across the FTO/m-TiO_2/PQDs/dye and which subsequently emits monochromatic green photofluorescence to re-excite the sensitizers. This device showed the impressive power conversion efficiency of 7.91%, well above the previous report in 2009.

2.3.1.4 Metal halide nanocrystals in silicon solar cells

Metal halide nanocrystals have been utilized for the improvement of the c-Si solar cell efficiency. Spherical organic-inorganic metal halide nanocrystals [214] and all-inorganic nanocubes [19] have been used for such purposes with the second showing the higher performance.

In the first case, a c-Si solar cell architecture based on a heterojunction between n-type c-Si and a conducting polymer (PEDOT:PSS) is demonstrated as an alternative concept of the field effect solar cell (Figure 5A). Usually, these solar cells consume extra electric energy originated from an external bias. In this case by introducing the perovskite nanocrystals, the extra potential is generated by the light [214]. The organometal trihalide nanocrystals synthesized by a low-temperature precipitation method are deposited on the top of the PEDOT:PSS top electrode and act as potential generation layer (Figure 5A). The device operates as a Schottky heterojunction solar cell with the light-induced electric polarization in the perovskite nanocrystals enhancing the electric field in the c-Si depletion region. The light harvested by organometal trihalide perovskite nanocrystals induces molecular alignment on a conducting polymer, which generates a positive electrical surface field. Photoinduced carriers generated in c-Si are directed to the respective contacts by the electric field in the depletion region at the interface between n-Si and MoO_3/PEDOT:PSS. The successful combination of the light-driving polarization perovskite nanocrystals with n-type c-Si leads to the fabrication of a “field-effect

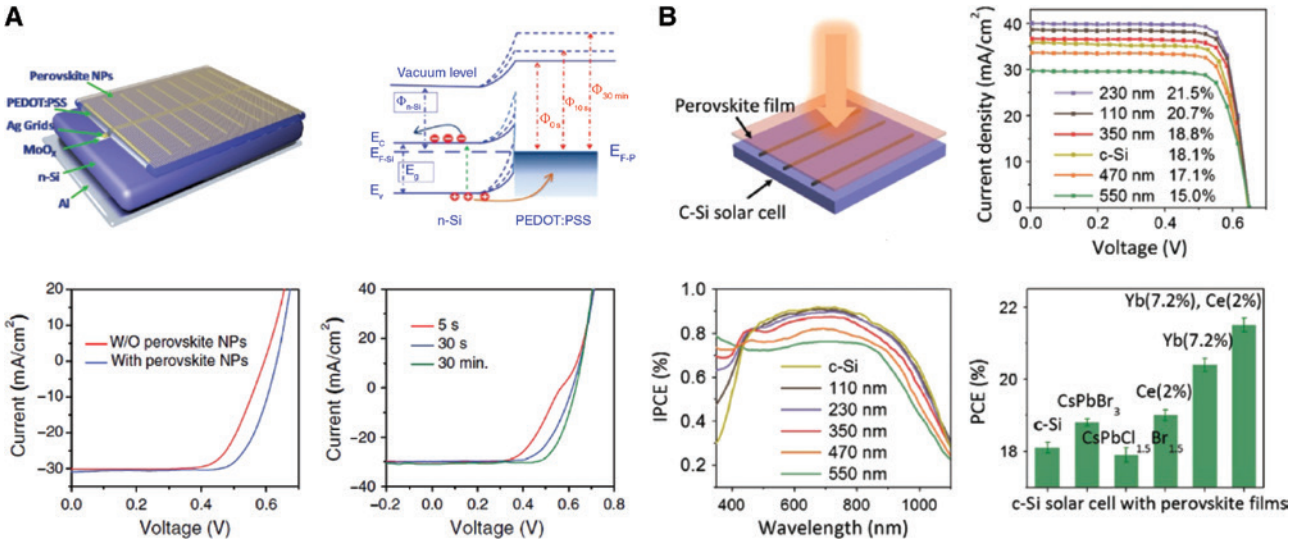

Figure 5: (A) "Field-effect solar cell" by using spherical hybrid organic-inorganic metal halide nanocrystals. Reproduced with permission from [214]. Copyright 2017, Wiley-VCH. (B) $CsPbCl_{1.5}Br_{1.5}$:Yb (7.1 %), Ce (2 %) perovskite nanocubes film, used as a downconverter in commercial silicon solar cells. Reproduced with permission from [19]. Copyright 2017, Wiley-VCH.

solar cell" with a PCE of 14.3%. This PCE showed a 12% enhancement compared to the one without using such nanocrystal coverage (12.7%). This device displayed a J_{sc} of 30.84 mA/cm^2, an FF of 73%, a V_{oc} of 635 mV, which results in a PCE of 14.3%. While the device without the perovskite nanocrystals exhibits a short circuit current (J_{sc}) of 30.42 mA/cm^2, an FF of 70%, an open circuit voltage (V_{oc}) of 594 mV, yielding a PCE of 12.7%.

The second report on using metal halide nanocrystals demonstrated a cheap, convenient, and effective way to enhance the PCE of the commercial silicon solar cells (Figure 5B) [19]. Doped all-inorganic metal halide nanocubes synthesized by a hot-injection method have been used as a downconverter of these solar cells due to their excellent quantum-cutting properties. The PCE in this case is improved from 18.1 to 21.5%. They were self-assembled on the surface of the commercial single crystal silicon solar cell via liquid-phase deposition and the thickness was controlled ranging from 60 to 770 nm. Compared to 18.1% PCE of the uncoated solar cells, the performance for the 110, 210, and 350 nm perovskite nanocrystals coated samples increases to different contents, while the further increasing thickness of the nanocrystals induces the decrease of solar cell performance. The best thickness of the nanocrystal layer is 230 nm. The PCE of this device reaches to 21.5%, with an open-circuit voltage 0.65 V and a short-circuit current 39.8 mA/cm^2 with good reproducibility. In the dark, the luminescent intensity of this layer is decreased less than 5% and the PCE decreased only about 5% after being placed in the air for 700 h, indicating a high stability. Irradiated by simulated AM 1.5 sunlight for 50 h continuously, the PCE is rarely changed, implying its excellent photostability. Finally, by testing various photoluminescent converters, the optimum enhancement of PCE was observed for the Yb^{3+}, Ce^{3+} co-doped perovskite nanocrystals. The PCE is comparable to the perovskite/silicon tandem solar cells but in this case the fabrication is easier and simpler to repeat.

2.3.1.5 Perovskite oxide nanocrystals in perovskite solar cells

Perovskite oxide nanocrystals have been used as electron transporting materials. Films of sol-gel synthesized nanocrystals of Zn_2SnO_4 have been utilized as ETLs for highly efficient perovskite solar cells [215]. There is a dual role of these materials in perovskite solar cells. On the one hand, the introduction of such films significantly improves the transmittance of flexible polyethylene naphthalate/indium-doped tin oxide (PEN/ITO)-coated substrate from ~75 to ~90% over the entire range of wavelengths and, on the other hand, due to its antireflection properties and low refractive index lead to the improvement of the PCE. The PCE in such perovskite solar cells leads the value of 14.85 % under AM 1.5G-100 mW/cm^2 illumination (Figure 6). Furthermore, by replacing them with hydrothermally synthesized Zn_2SnO_4 nanocrystals the performance has been further increased to a PCE of 17.7% [20]. These materials were characterized by high electron

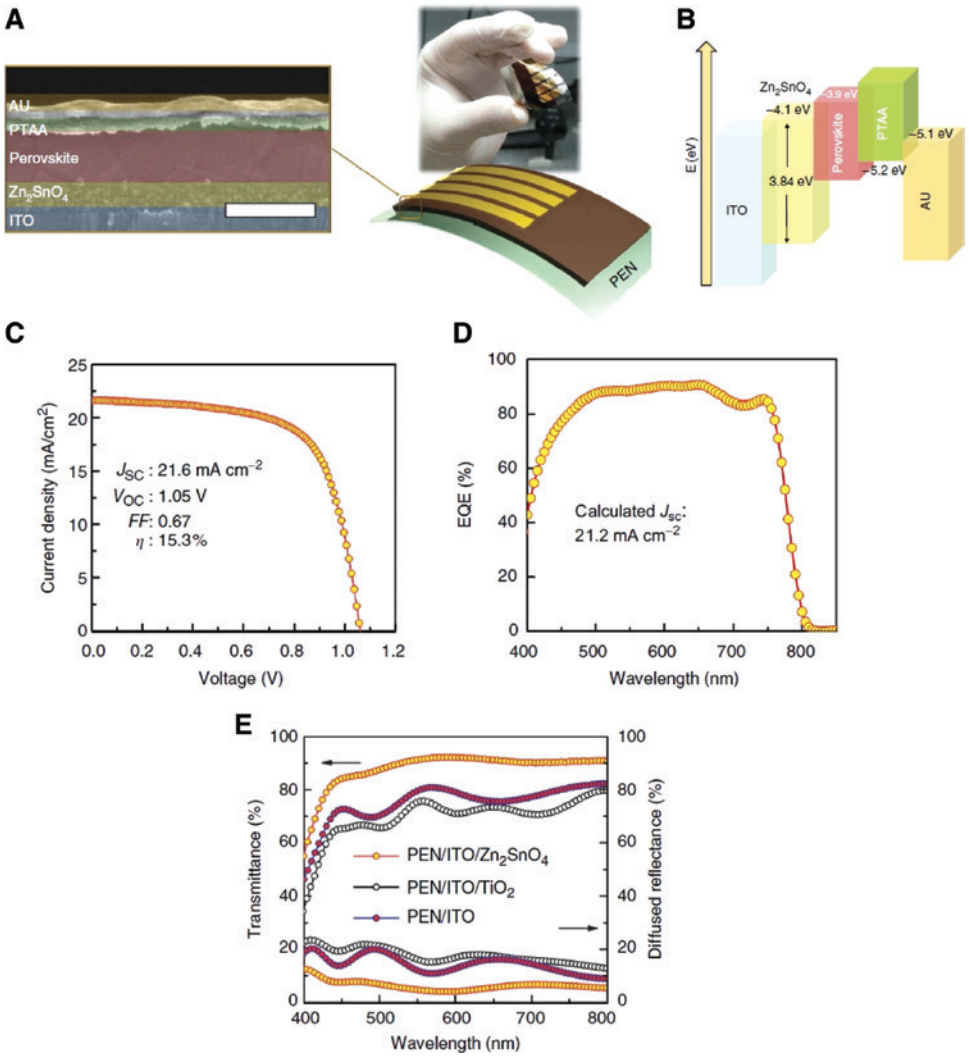

Figure 6: Structure and performance of flexible perovskite solar cells including Zn_2SnO_4 nanocrystals as hole transporting layer. Cross-sectional SEM image and photograph of the ZSO-based flexible perovskite solar cell (scale bar, 500 nm) (A). Energy levels of the materials (B). Photocurrent density–voltage (J–V) curve measured by reverse scan with 10 mV voltage steps and 40 ms delay times under AM 1.5 G illumination (C). EQE spectrum of the ZSO-based flexible perovskite solar cell (D). Transmittance and reflectance spectra of PEN/ITO/ZSO, PEN/ITO/TiO_2 and PEN/ITO substrate (E). Reproduced with permission from [215]. Copyright 2015, Nature Publishing Group.

mobility of 10–25 cm^2/Vs, a wide optical bandgap (3.8 eV), and a well-aligned conduction band edge (~– 4.1 eV) with that of the absorbing layer ($CH_3NH_3PbI_3$).

2.3.1.6 Perovskite oxide nanocrystals in dye-sensitized solar cells

Quite spherical perovskite nanocrystals have been used in ETL in dye sensitized solar cells due to their superior electron collection property. The energy conversion reported for such solar cells is 4.7% for using Zn_2SnO_4 [152] and 5.2% for $BaSnO_3$ [216] nanocrystals. The electron capture in the perovskite oxide films was higher than in TiO_2 and the electron in the conduction band can diffuse rapidly resulting in greater photovoltaic performance.

2.3.2 Perovskite nanocrystals for photocatalytic CO_2 reduction in solar fuel cells

The emission of CO_2 by human activities is an important factor for the dramatic change of the environment and phenomena such as the climate change and global warming. Photocatalytic reduction of CO_2 using solar energy into renewable hydrocarbon fuels has gained much attention in the effort to conserve energy [21]. By

mimicking the natural photosynthesis in green plants, artificial conversion of CO_2 into chemical fuels such as carbon monoxide [CO], methane [CH_4], methanol [CH_3OH], offers a promising approach to simultaneously mitigate the levels of greenhouse gas and produce renewable energy. Nanocrystals of metal halides or perovskite oxides have been introduced as efficient photocatalysts for such purposes.

2.3.2.1 Metal halide nanocrystals for photocatalytic reduction of the CO_2

Metal halides have not been applied for photochemical conversion (water splitting or CO_2 reduction) due to their instability in the presence of moisture or polar solvents. But there are some recent reports on novel photocatalysis to convert CO_2 into solar fuels in non-aqueous media. Single-phase lead-containing or lead-free metal halide nanocrystals have been proposed as novel catalysts for solar cell CO_2 reduction. $CsPbBr_3$ quantum dots with diameters 3–12 nm showed a highly selectivity over 99% and achieve an efficient yield rate of 20.9 μmol/g towards solar CO_2 reduction (Figure 7A). [22] While lead-free nanocrystals of $Cs_2AgBiBr_6$ showed an impressive stability against moisture, light, and temperature and under AM 1.5G illumination for 6 h achieved a total electron consumption of 105 μmol/g [23].

Enhanced photocatalytic reduction of CO_2 to ethyl acetate observed when $CsPbBr_3$ quantum dots are coupled with GO (Figure 7B) [24]. Under AM 1.5G simulated illumination, the primary $CsPbBr_3$ nanocrystals of 6 nm in diameter steadily generated and injected electrons into CO_2, catalyzing CO_2 reduction at a rate of 23.7 μmol/g h with the important selectivity over 99.3%. The growth of the perovskite on GO results in the increase of the electron rate to 25.5% due to the improved electron extraction and transport. These rates are superior compared to the common CdS quantum dots photocatalysts. These photocatalysts

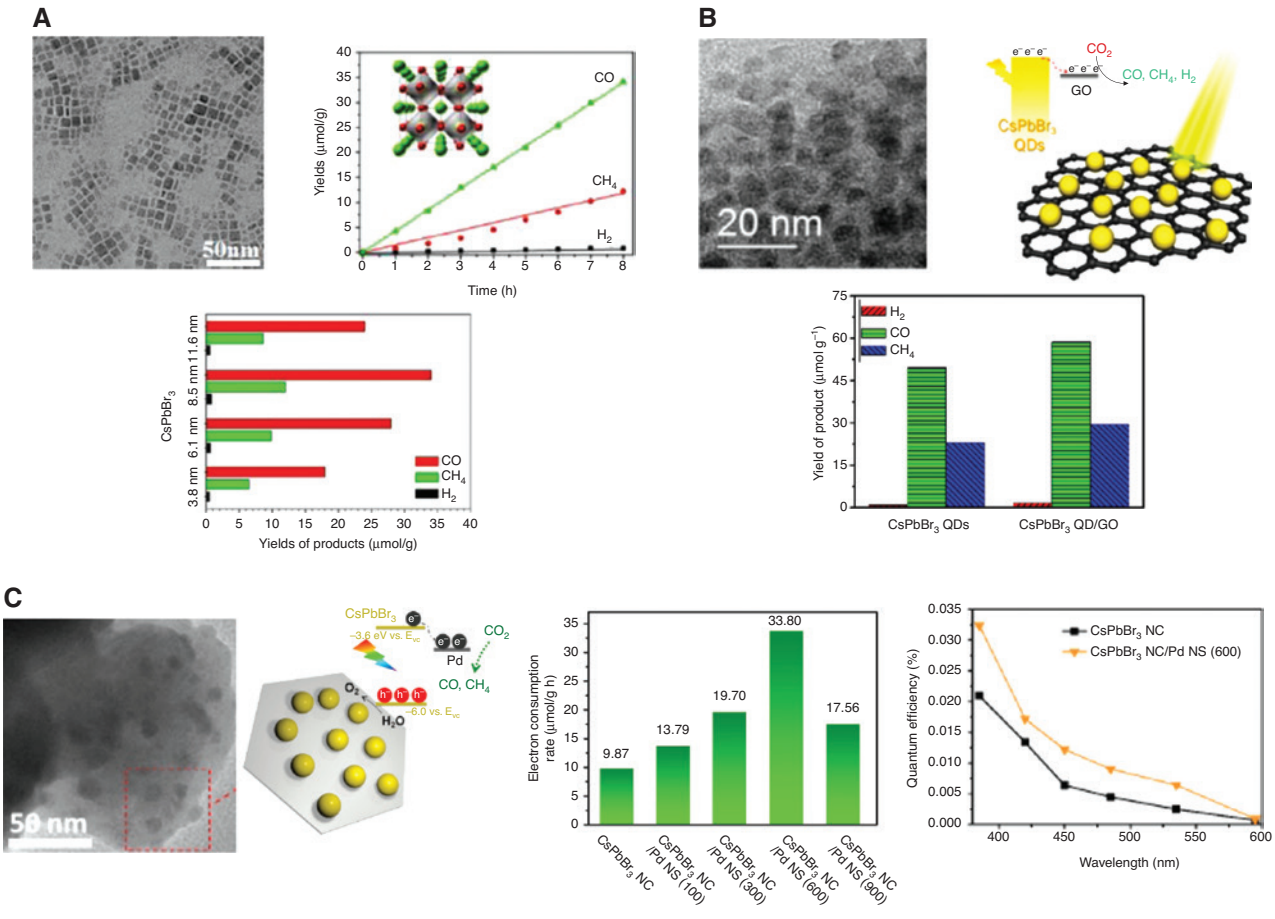

Figure 7: Metal halide nanocrystals for photocatalytic CO_2 reduction.
(A) Single phase $CsPbBr_3$ nanocatalysts. Reproduced with permission from [22]. Copyright 2017, Wiley-VCH. (B) Composite $CsPbBr_3$/GO catalysts. Reprinted with permission from ref [24]. Copyright (2017), American Chemical Society. (C) Composite $CsPbBr_3$/Pd catalysts. Reprinted with permission from [217]. Copyright (2018), American Chemical Society.

are stable after 12 h of photocatalytic reaction and no phase transformation or degradation are observed. The effective CO_2 reduction capacity (1.05 μmol/cm² h) and selectivity (84%) are much smaller in the case of nanocomposites including hybrid organic-inorganic metal halide nanocrystals and GO [25]. The photocatalytic performance of the previous nanocomposite is improved when the metal halide nanocrystals were coupled with palladium nanosheets instead of GO (Figure 7C) [217]. Their optimized performance in this case was 33.79 μmol/g h, corresponding to 2.43-fold enhancement compared to the pristine metal halide nanocrystals.

Furthermore, the encapsulation of the $CsPbBr_3$ nanocrystals in amorphous-TiO_2 showed a marvelous 6.5-fold improvement on the consumption of photoelectrons in photocatalytic CO_2 reduction reactions compared to that of individual $CsPbBr_3$ nanocrystals [218]. Despite the poor photocatalytic behavior of the amorphous TiO_2, its good chemical stability makes it good candidate as a protection layer for the lead halides. The amorphous TiO_2 coverage has been witnessed as a pivotal driving force for preeminent photocatalytic performance by enhancing the extraction and separation of the photoinduced charges, and increasing the adsorption of the CO_2 simultaneously. Such combined effects finally boost the photoelectron consumption from 25.72 to 193.36 μmol/g during the 3 h photocatalytic reaction. Photocatalytic reduction of CO_2 to CH_4 is more thermodynamically favorable than the formation of CO and H_2, which however, is kinetically challenging since eight electrons were involved.

2.3.2.2 Perovskite oxide nanocrystals for photocatalytic reduction of the CO_2

$NaNbO_3$ and $NaTaO_3$ nanocrystals of similar size and synthesized by the same method have been tested as photocatalysts for the reduction of the CO_2 [219]. Both perovskites give rise to the similar conversions in the CO_2 reduction reaction with a slightly higher carbon product evolution for the nanocrystals of $NaTaO_3$. Furthermore, the crystal structure of the nanocrystals seems to be a crucial factor for the photoreduction performance of the $NaNbO_3$ nanocrystals [220]. The photocatalytic H_2 evolution and CO_2 reduction activities over cubic $NaNbO_3$ were nearly twice of those over orthorhombic $NaNbO_3$ structure. The electronic structure of the cubic phase is beneficial for electron excitation and transfer. Furthermore, nanowires of the same chemical structure covered with the polymer g-C_3N_4 showed an enhanced photocatalytic performance (8 times higher) compared to the single-phase g-C_3N_4 or the $NaNbO_3$ nanowires [221]. The remarkable enhancement of photocatalytic activity was mainly ascribed to the improved separation and transfer of photogenerated electron-hole pairs at the intimate interface of g-C_3N_4/$NaNbO_3$ heterojunctions, which originated from the well-aligned overlapping band structures of C_3N_4 and $NaNbO_3$. Finally, $KNbO_3$ (where A=Na, K) nanocrystals showed a higher photocatalytic activity compared to the $NaNbO_3$ due to its narrower band gap and higher mobile charge carriers [222].

$BiWO_6$ nanocrystals of different morphologies have been synthesized for photo-induced CO_2 reduction. Square $BiWO_6$ nanoplateles of 9.5 nm in thickness and capped with oleylamine were used for such purposes [223]. Their enhanced catalytic activity is due to the preferentially exposed {001} surface. The ultrathin geometry of these nanocrystals also promotes charge carriers to move rapidly from the interior to the surface to participate in the photoreduction reaction and should also favor an improved separation of the photogenerated electron and hole and the lower electron-hole recombination rate. More complex nanosheet-based nanocrystals have been also designed to improve the catalytic performance. Ball-flower-like nanostructures composed by nanoplatelets [224] or nanoplatelets decorated with core-shell Au-CdS [225] also synthesized for such purposes.

2.3.3 Perovskite nanocrystals for thermoelectrics

Generating energy through thermoelectric materials is becoming increasingly important as the challenges faced nowadays in terms of energy production and efficiency are more intense than ever. Much work has been carried out during the past decades in an effort to enhance the production of energy through novel materials and processes [226–228].

Thermoelectric generators (TEG) constitute a new technology in order to recover heat which is based on the Seebeck effect and is broadly used for power generation. The Seebeck effect can be described as the connection of two different type (p-type and n-type) of conductors or semiconductors. This connection is formed by a parallel thermal connection along with an electrically connection in series which in turn causes a difference in voltage between the two materials [229, 230]. When connecting the two different components with a heated junction one can observe on the n-type component the transport of electrons from the hot junction to a heat sink whereas the p-type component transports holes which are positively charged, following the same direction as the temperature gradient.

The efficiency that a specific material can possess in the conversion process of heat to electricity can be given by the formula below.

$$ZT = \frac{\alpha^2 \sigma T}{\kappa} \quad (1)$$

where ZT is the dimensionless figure of merit, σ is the electrical conductivity of the material, κ is the thermal conductivity of the material and α the Seebeck coefficient [231, 232].

In order for thermoelectric materials to be competitive with ordinary power generators the figure of merit for TEG must be larger than 3 [233, 234]. Generally, finding materials with a ZT value above 2 is a challenging task but recent advancements [235, 236] in the effort to increase the figure of merit to around 3 has been made possible with the use of nanocomposites.

In this direction, lead and tin halide perovskites namely $CH_3NH_3PbI_3$ and $CH_3NH_3SnI_3$ have been regarded as very promising photovoltaic materials mainly because of their relatively large absorption coefficient, high charge carrier mobility, and diffusion length properties [212, 237] also possessing a large Seebeck coefficient [238, 239]. Recent first principle studies of these materials have confirmed this and have provided detail insides especially when results are combined with the Rashba effect.

Recently Nafradi's group has also shown that the ZT of the Sn component of the hybrid halide perovskite mentioned can be augmented by three orders of magnitude at room temperature by appropriate chemical doping [240]. This finding suggests that $CH_3NH_3SnI_3$ can constitute a very promising candidate for low cost and mass production processes.

Similar improvement in the thermoelectric properties of perovskites was observed with W doping for $CaMnO_3$ by Tan's group [241]. They reported a two-fold increase in the figure of merit which in turn is attributed to structural characteristics involving the existence of MnO_6 distorted octahedra. This case is also interesting as two mechanisms are reported to occur simultaneously although their effect is canceling one another. The W doping seems to increase carrier concentration which ultimately leads to enhanced electrical conductivity and a decreased Seebeck coefficient. The enhanced electrical conductivity is a positive effect that outweighs the negative impact of the decreased Seebeck coefficient thus leading to an increased power factor. This increase in ZT is also temperature depended and seems to increase almost linearly with increasing temperature.

Overall the structural dependence of the ZT still remains a big challenge and is a promising field for more intensive research in order to elucidate the structural dependence of the above-mentioned phenomena.

2.4 Perovskite nanocrystals for energy storage

2.4.1 Perovskite nanocrystals for batteries

Emerging autonomous electronic devices require compaction and miniaturization of energy storage devices. Perovskite materials have received considerable attention for energy storage applications due to their excellent catalytic activity, electrical conductivity, and durability. Ion migration through perovskite lattices allowing the use of such materials as electrodes for batteries. Electrochemical measurements on nanoparticulate perovskite systems showed that they displayed superior catalytic activity for oxygen reduction, as well as a higher discharge plateau and specific capacity compared to the bulk materials of the same crystal structure [29]. Perovskite oxide nanocrystals have been investigated for such application but in recent years metal halides have also shown high specific capacitance and promising stability upon cycling. This section summarizes all the reports on such applications focused on nanoparticulate systems of both metal halides and perovskite oxides and tries to correlate and understand the role of the size, the morphology and the intrinsic properties of the nanocrystals to the final performance of the batteries.

2.4.1.1 Metal halide nanocrystals in batteries

The first report of using metal halide materials for Li-ion batteries was in 2015 by Peng's group [30]. Hydrothermally grown organic-inorganic metal halide microcrystals were used as the active material in Li-ion storage devices presenting a discharge capacity of 331.8 mA h/g (at current density of 200 mA/g) [30]. In this system, the capacity decreased rapidly in the first 30 cycles, it subsequently decayed slowly, showing a relative capacity retention of 76.9 % in the next 170 cycles. A comparison between different halides indicated that the batteries with the $CH_3NH_3PbBr_3$ showed a larger discharge capacity compared to that with $CH_3NH_3PbI_3$. The discharge capacity for the first system was 331.8 mA h/g while for the second only 43.6 mA h/g. Two years later, $CH_3NH_3PbBr_3$ nanocrystals of 65 nm in size, synthesized by a precipitation method combined with a heating process, showed similar electrochemical response (Figure 8A) [31]. Long-term specific capacity attained significant values,

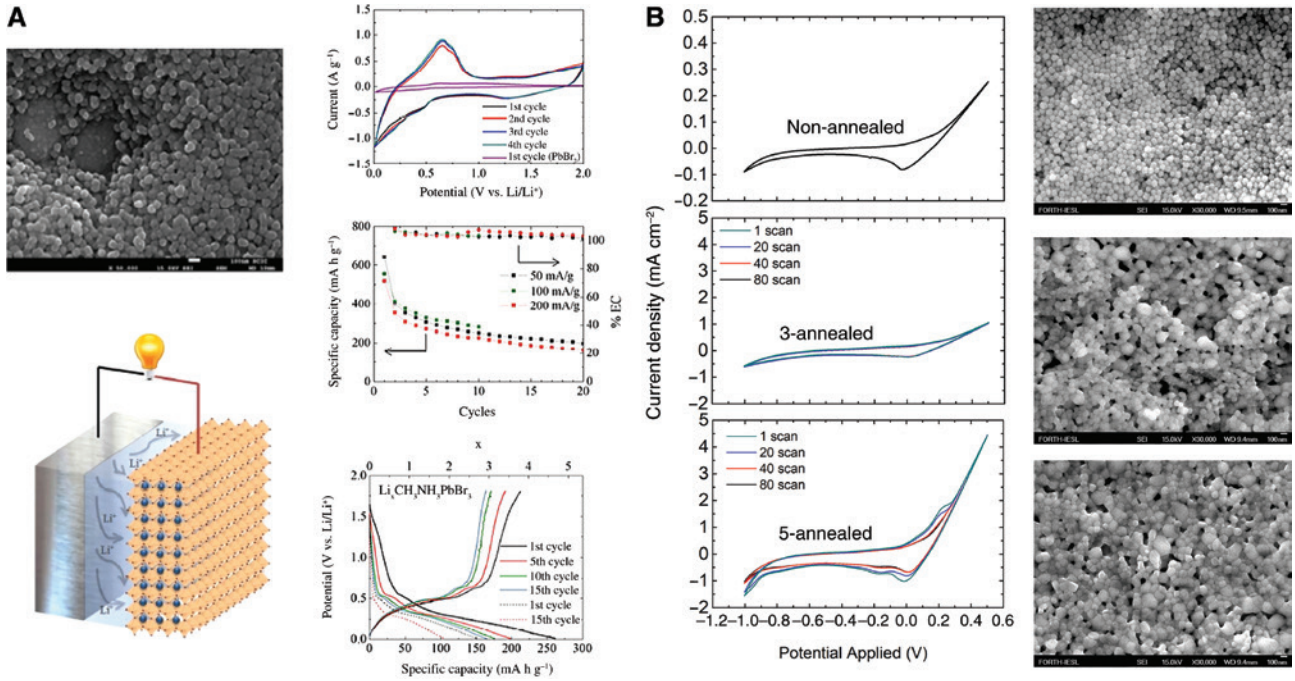

Figure 8: Metal halide perovskite nanocrystals for Li-air batteries. Electrochemical performance of the anodes consisted of (A) hybrid organic-inorganic $CH_3NH_3PbBr_3$ nanocrystals of 65 nm in size, synthesized by a precipitation method combined with a heating process and (B) all-inorganic metal halide, Cs_4PbBr_6 nanohexagons of 100 nm in size deposited on ITO electrodes and subjected to three and five cycles of thermal annealing. These layers are coated with a few-nanometer thin TiO_x layer. (A) Reprinted with permission from [31]. Copyright (2017), American Chemical Society. (B) Reproduced from [32] with permission from the Royal Society of Chemistry.

approaching 200 mA h/g. Very recently, the electrochemical performance of metal halide nanoparticulate electrodes by using aqueous electrolyte were evaluated by our group [32]. This is the first report of using metal halide nanocrystals in batteries using aqueous electrolytes. In particular, the electrodes comprised a layer of 100 nm-size Cs_4PbBr_6 nanohexagons deposited on ITO substrates and coated with a thin TiO_x film (Figure 8B) [32]. The nanocrystals were prepared at room temperature, by a fast, solution-processed co-precipitation method. The electrodes were subjected to successive annealing cycles to optimize their electrochemical stability. The electrodes of five annealing cycles showed the best performance. It was observed that these electrodes showed the best performance among the nanoparticulate anodes using metal halides presented previously in terms of stability (high stability for 40 scans), specific capacity (377 mA h/g) and coulombic efficiency (dropped to 98% after 100 scans). On the contrary, the non-annealed and/or uncoated nanohexagon layers displayed poor stability, immediately after the first scan. A water-triggered transformation of the metal halide material occurred in the aqueous medium from Cs_4PbBr_6 to $CsPb_2Br_5$. Then, the Li-ion intercalation/deintercalation mechanism is a reversible process for the 40 consecutive scans, as the crystal structure of the $CsPb_2Br_5$ remains unaltered. After this period, an irreversible conversion reaction of $CsPb_2Br_5$ to CsBr and $PbBr_2$ occurs up to 100 scans.

The overall capacity of the batteries is strongly dependent on the accessibility of the host material interior to the ions [242]. Different mechanisms Li^+ intake/release have been proposed for the metal halides in order to explain the different final performance of the devices. Topotactic insertion into organic-inorganic metal halide host ($CH_3NH_3PbBr_3$) has been proposed by Garcia-Belmonte's group [31]. Non-drastic structural alterations or rearrangements in the crystal lattice have been observed in this case. A different mechanism was proposed by Islam's group for the same anode material. Using a combination of density functional theory and results by means of electrochemical characterization and diffraction techniques [243], Li intercalation and conversion reactions in the $CH_3NH_3PbX_3$ (where X: Br, Cl, I) take place. The conversion process with the production of CH_3NH_3X, lithium halides (LiX), and Pb metal was found to be energetically more favorable than Li intercalation. Furthermore, it was also found that the specific capacity is dependent on the

crystal structure of the perovskite material [244]. This could be improved by changing the dimensionality of the halide perovskites from three-dimensional (3D) to a one-dimensional (1D) lattice [245]. Indeed, experiments on organic-inorganic hybrid lead halide perovskites showed that the Li intercalation in the two-dimensional (2D) tetragonal structure is enhanced compared to the 3D orthorhombic one, due to the larger cell volume [243]. Finally, the type of the anion plays role in the charging performance [243]. It is observed that the Li intercalation is more favorable in the case of the iodides than in the chlorides or bromides [245].

2.4.1.2 Perovskite oxide nanocrystals in batteries

The perovskite oxide nanocrystals started to be used in batteries from 2014. The first nanocrystals were from $LaNi_{1-x}Mn_xO_3$, $La_{0.6}Sr_{0.4}CoO_3$ and $Ba_{0.9}Co_{0.5}Fe_{0.4}Nb_{0.1}O_{3-\delta}$ chemical phases and succeed to be stable for less than 50 battery cycles [132, 246, 247]. Later in 2016, $LaNiO_3$ nanoparticles showed an improved cycling ability up to 155 cycles [248]. Single phase nanocrystals such as spherical or randomly-shaped [33, 34, 36, 132, 246–253], nanocubes [147], and anisotropic ones [38–41, 254, 255] or bifunctional structures such as core-shell morphologies [42], decorated structures with a second material (metal, carbon, or oxides) [43–45], or composites [46] have been tested in order to improve the catalytic performance in batteries. Except the size and the morphology, there are other factors that affect the electrochemical performance in the case of the perovskite oxides such as the structural nanocrystal quality and the existence of defects in the lattice [33], the doping in the A and/or B site of the perovskite lattice [34–37], the nanocrystal porosity [38–41] and the existence of synergetic effects in the bifunctional morphologies [42–46].

For example, nanocrystals synthesized by a ball-milling process showed superior catalytic activities compared to the nanocrystals without this process due to the structural change and defects in the crystal structure [33]. B-site doping in the manganite perovskite oxides ($La_{0.8}Sr_{0.2}Mn_{1-x}Ni_xO_3$) showed enhanced performance compared to the undoped one due to the introduction of more oxygen vacancies at the surface (Figure 9A) [252]. The capacity can be tuned by doping in the A site of the perovskite and decreased from 7211 to 6205, 6760, and 5925 mA h/g for $La_{0.65}Pb_{0.35}MnO_3$, $La_{0.65}Ba_{0.35}MnO_3$, $La_{0.65}Sr_{0.35}MnO_3$ nanocrystals respectively [34]. The effect of the doping in the B-site has been studied in the La-based perovskite oxides and showed that the performance is improved in the order of $LaCrO_3$, $LaFeO_3$, $LaNiO_3$, $LaMnO_3$, and $LaCoO_3$ [37].

The morphology and also the porosity of the nanostructures affect the electrochemical performance, including the first discharge specific capacity, the overpotential, the rate capability, and the cycle stability. The enhanced performance is due to the formation of direct current pathways that facilitate electron transport, short O_2^{2-}/Li^+ diffusion lengths that can improve ion transferring rates to oxygen electrode, the existence of a more efficient electrolyte-electrode contact, the increase of active sites for ORR/OER during battery operation, and the existence of more space to store discharged products. [38]. Porous nanocubes (Figure 9B) [147] or elongated nanocrystals (nanorods or nanotubes or nanofibers) [39–41, 256] of perovskite oxides have been introduced for such purposes. Furthermore, bifunctional nanocrystals have been utilized to enhance the performance in metal-air batteries. Synergetic effect have been utilized to improve the catalytic activity by covering the $La_{0.8}Sr_{0.2}MnO_3$ nanorods with a layer of $NiCo_2O_4$ [42]. The ORR takes place mainly at the core, while the OER takes place at the nanoscale shell and their synergetic effect leads to the enhanced catalytic performance. Synergetic effects have also been observed in different bifunctional morphologies such as perovskite oxide nanocrystals decorated with nitrogen-doped carbon nanotubes [43], perovskite nanorods/graphene composite decorated with Ag nanocrystals [46], perovskite nanofibers functionalized with RuO_2 nanoparticles and non-oxidized graphene nanoflakes [44], perovskite porous nanofibers loaded with RuO_2 nanosheets (Figure 9C) [45].

2.4.2 Perovskite nanocrystals for supercapacitors

Perovskites have found also use as electrode materials in supercapacitors for energy storage. A simple design of a supercapacitor is based on two electrodes separated by an ion-permeable membrane and an electrolyte ionically connecting to both electrodes. During the polarization of the electrodes the ions are moving to oppose the electrode's charges, forming electric double layers of opposite polarity. Supercapacitors are divided into three categories, the double-layer capacitors where the charge storage is electrostatically, the pseudocapacitors with electrochemically charge storage, and the hybrid ones which combine electrostatically and electrochemically charge storage [257]. The nanodimensional perovskites that are used for such purposes are some metal oxides, a few nanocomposites and even more limited halides in contrast with the many reports for using all-inorganic or hybrid halides in photovoltaic applications. Many studies have been reported in lanthanum-based perovskite nanocrystals

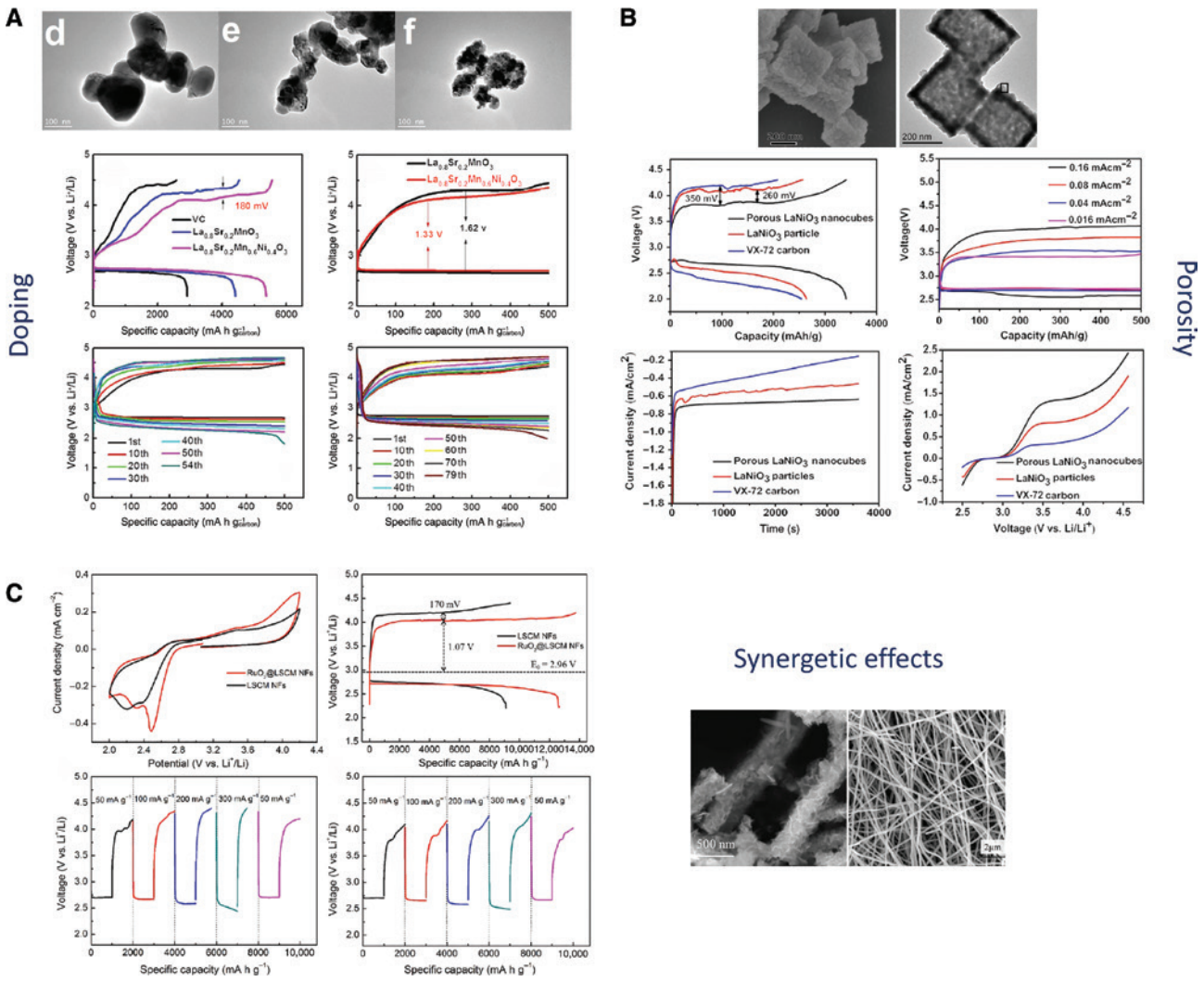

Figure 9: Electrochemical performance of Li-air batteries including perovskite oxide nanocrystals. Three factors that affect this performance are: Ni-doping in manganite perovskite oxide (A), porosity of the nanocrystals ($LaNiO_3$ nanocubes) (B), and synergetic effects in bifunctional nanocrystals ($La_{0.6}Sr_{0.4}Co_{0.8}Mn_{0.2}O_3$ nanofibers loaded with RuO_2) (C).
(A) Reprinted with permission from [252]. Copyright (2016), American Chemical Society. (B) Reproduced with permission from [147]. Copyright 2014, Springer. (C) Reprinted with permission from [45]. Copyright (2017), American Chemical Society.

due to their structural stability at high temperatures and inherent nature to contain oxygen vacancies. Additionally, the structure of lanthanum-based perovskites allows the substitution of ions by other ions of varying oxidation states changing on demand the electronic and physical properties [258]. Specifically, in $LaMnO_3$ nanocrystals by tuning the oxygen content, capacitance of 586.7–609.8 F/g has been achieved [258]. Introducing a secondary phase of La_2O_3 attached on the nanocrystals could result in the capacitance of 520 F/g [259]. Important also is the substitution of the B site (ABO_3) in the perovskite crystal structure with elements such Mn, Fe, Cr, and Ni which leads to capacitances of 56.78, 16.43, 24.4, and 106.58 F/g, respectively, after 500 charge-discharge cycles in a 3 M LiOH solution [260]. Furthermore, among the lanthanum-based candidates for supercapacitors the perovskites with Ni in the B site hold a prominent role. The incorporation of Ni offers excellent electrical conductivity and presents capacitances of a few hundred F. Specifically, $LaNiO_3$ nanosheets [49], hollow nanospheres [48], and randomly-shaped nanocrystals [261] exhibit capacitance of 139.2 mA h/g (at 1.0 A/g), 422 F/g (at 1.0 A/g), and 478.7 F/g (at 0.1 mV/s), respectively, while their cycling stability reaches the 10000, 5000, and 15000 cycles, respectively. Figure 10 shows their morphology and the cyclic voltammetry curves at different scan rates.

A different type of lanthanum-based supercapacitor is that of incorporating composite materials. In this

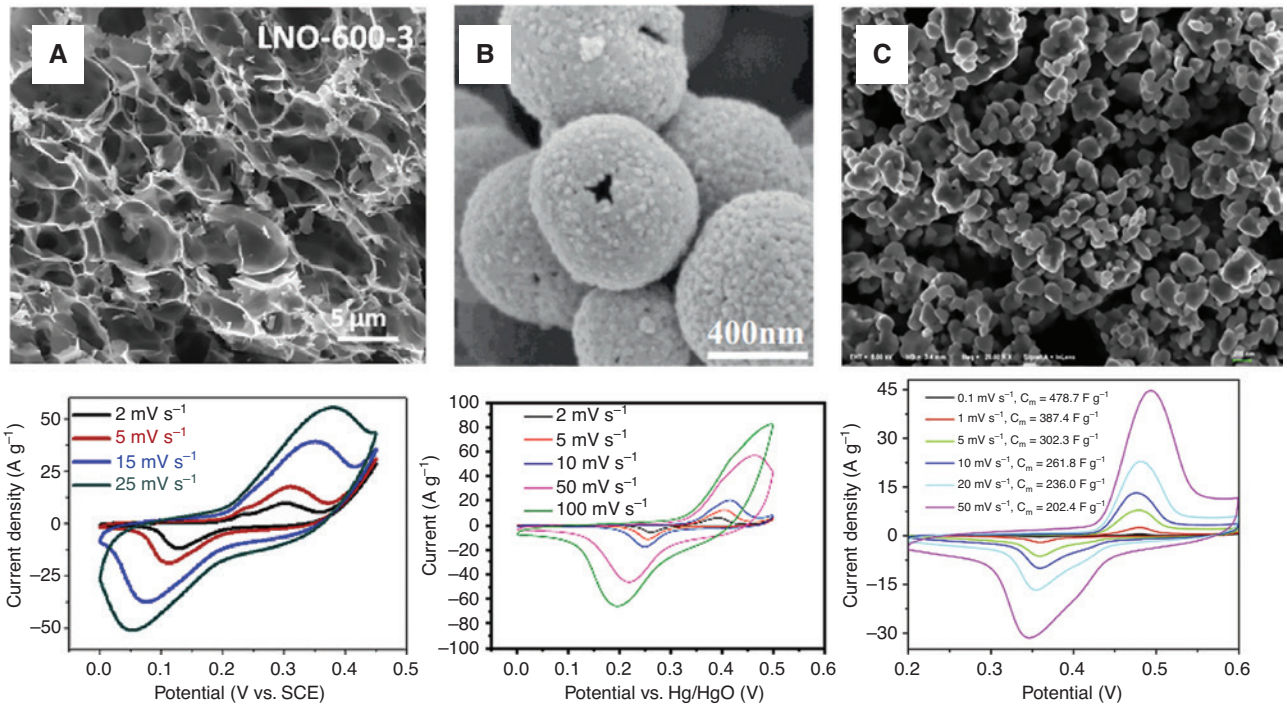

Figure 10: $LaNiO_3$ perovskite nanocrystals for electrodes in supercapacitors with morphologies; (A) nanosheets, (B) hollow nanospheres, (C) irregular-shaped nanocrystals (above figures) and their cyclic voltammetry measurements at different scan rates (below figures). (A) Reproduced with permission from ref [49]. Copyright 2017, Elsevier. (B) Reproduced with permission from ref [48]. Copyright 2017, Elsevier. (C) Reproduced with permission from ref [261]. Copyright 2018, Elsevier.

direction, a promising nanocomposite is the CeO_2 mixed $LaMnO_3$ which has been assessed as a negative electrode material [262]. The advantage of such a mixture is the high surface to volume ratio of the CeO_2 nanocrystals which increases the active sites of the electrode. During the three-electrode measurement, the supercapacitor displayed 262 F/g for 1 A/g, retaining the 98% of capacitance after 2000 cycles. Another interesting nanocomposite system is that which combines the $LaMnO_3$ with nitrogen-doped reduced graphene oxide (N-rGO). Doping the rGO with an amount of 25% of N-rGO, the active material exhibits 687 F/g at 5 mV/s and retains stability of 79% after 2000 cycles [263]. While the nanocomposite $LaMnO_3$@Mn_3O_4 demonstrates remarkable stability of the specific capacitance even in 50,000 cycles (135 F/g at 1 A/g) with a maximum energy density of 75 W h/kg.

In addition, the substitution of La atoms in the crystal structure of the perovskite with Sr gives very high specific capacitances. According to this, $La_{0.7}Sr_{0.3}CoO_{3-\delta}$ nanofibers [47] or $La_{0.85}Sr_{0.15}MnO_3$@$NiCo_2O_4$ (LSM15@NC) nanoflowers [264] have shown 747 F/g (in Na_2SO_4 electrolyte at 2 A/g current density) and 1341 F/g (in 6 M KOH at 0.5 A/g current density), respectively. These values are among the highest reported for perovskites (Figure 11). In the case of the nanofibers, the substitution of La with Sr^{2+} into $LaCoO_3$ lattice induces more oxygen vacancies which are active sites for storage in pseudocapacitive applications. Similar mechanism takes place in the LSM15@NC perovskites. Remarkably, the LSM15@NC nanocomposite in an asymmetric supercapacitor delivers energy density of 63.5 W h/kg at the power density of 900 W/kg. This energy density is higher than those recorded for Ni, Co, and/or Mn-based asymmetric capacitors [264]. The specific capacitance also increases slowly for the first 3000 cycles, becomes double above the 3000 cycles up to 10000 cycles. This indicates the efficiency of this material for high performance supercapacitors.

Bimetallic Co-Mn and Ni-Co perovskite fluorides are also promising electrode materials for supercapacitors. $KCo_xMn_{1-x}F_3$ with Co:Mn 6:1, governed by strong synergistic effect of Co/Mn redox species exhibited a specific capacity of 226–192 F/g at 1–16 A/g coupled with a cycling stability of 5000 cycles (at 8 A/g). In an asymmetric capacitor design, it delivers 8–2.4 W h/kg at 0.14–8.7 kW/kg retaining the 90% of capacity in 10,000 cycles at 5 A/g [265]. While the similar structure with Ni, $KNi_{0.8}Co_{0.2}F_3$ nanocrystals showed an energy density of 42.7–13.8 W h/kg at 0.242–18.8 kW/g power density [266].

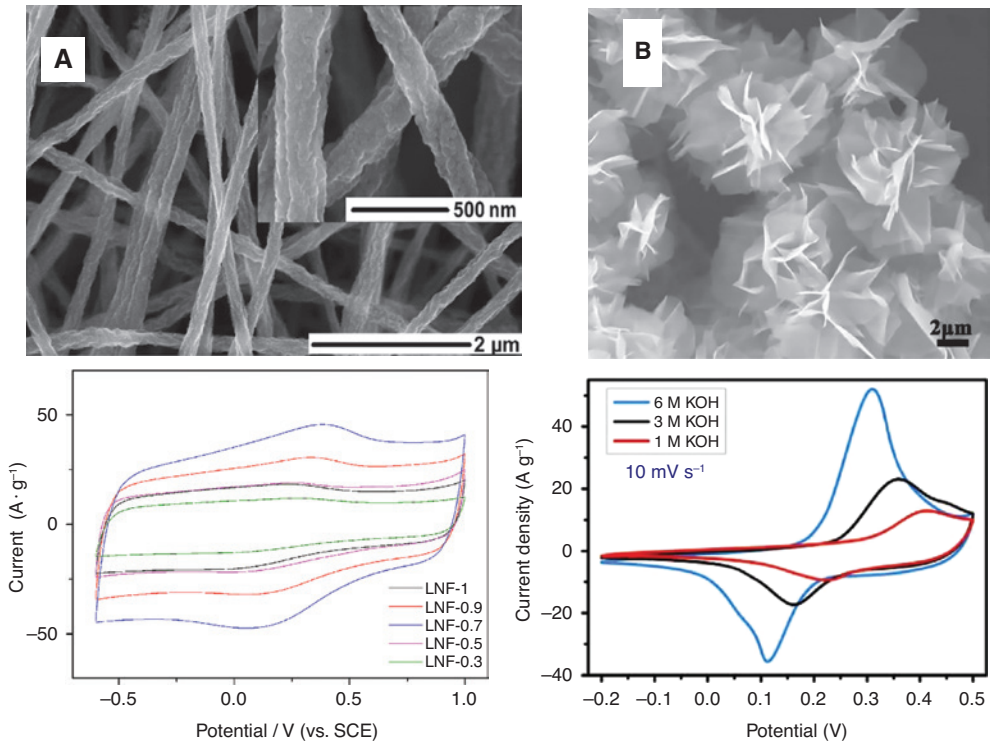

Figure 11: SEM images (above figures) and cyclic voltammograms (below figures) for (A) $La_{0.7}Sr_{0.3}CoO_{3-\delta}$ nanofibers, (B) $La_{0.85}Sr_{0.15}MnO_3$@ $NiCo_2O_4$ nanoflowers.
(A) Reproduced with permission from [47]. Copyright 2015, Elsevier. (B) Reproduced with permission from ref [264]. Copyright 2018, Elsevier.

Various oxide nanocrystals different than the previous have also been introduced for supercapacitor applications. Among these, $BiFeO_3$ nanocrystalline porous film showed a capacitance of 81 F/g [267], $BiFeO_3$ nanoplates 254.6 F/g [268], Y_2NiMnO_6 nanowires 77.76 F/g [269], $LaFeO_3$ nanocrystals with Na and Mn substitutions 56.4 F/g [270], doped $SrMnO_3$ nanofibers 321.7–446.8 F/g depending the doping of Ba/Ca on Sr and Co/Fe/Ni on Mn [271], $SrTiO_3$ nanocubes with Co doping 75.28 F/g [272] and nano-Ru-based perovskites on rGO 564-316 F/g [273].

2.4.3 Perovskite nanocrystals for hydrogen storage

Hydrogen, the most sustainable fuel offering higher efficiencies compared to diesel and gasoline, is compatible with fuel cells and produces renewal waste (i.e. water). There are various hydrogen storage methods such as gas compression or liquefaction, however, they face safety issues. The most safe approach is the storage in solid-state materials such as metal alloys, metal oxides, hydroxides, carbon, chalcogenides, and recently in perovskites [51]. The perovskite powders were reported in 2004 by Esaka's group as new anode materials for a hydrogen battery [274]. Later, in 2010, $LaFeO_3$ and $LaCrO_3$ powders were proposed as negative electrodes for Ni/MH batteries by Chen's group [275, 276].

Three years later, Chen's group succeeded in improving the electrochemical kinetics of the $LaFeO_3$ perovskites by nanostructuring. These nanocrystals formed aggregates with sizes ranging from 50 to 100 nm [50]. The nanocrystals showed a higher discharge capacity than the bulk counterparts of the same stoichiometry. The discharge capacity is a value which characterizes the hydrogen storage efficiency of a material and it is estimated by the galvanostatic behavior of charge and discharge. In this method the investigated material was deposited on the electrode and circles of charges and discharges were followed [51]. In the case of nanostructured $LaFeO_3$, the discharge capacity reaches the value of 531.5 mA h/g for 333 K for the first cycle (Figure 12A), degraded and stabilized above 350 mA/g for 20 cycles (a bit higher than the bulk). However, the $LaFeO_3$ nanostructures showed higher current densities and hydrogen diffusion coefficients. Decreasing the size of the nanostructures is expected to increase the discharge capacity due to the larger surface area. A different perovskite system which tested for its H_2 storage capability was the $DyFeO_3$ nanocrystals reported by Salavati-Niasari's group [277]. These nanocrystals have a size around 16–18 nm and showed a discharge capacity

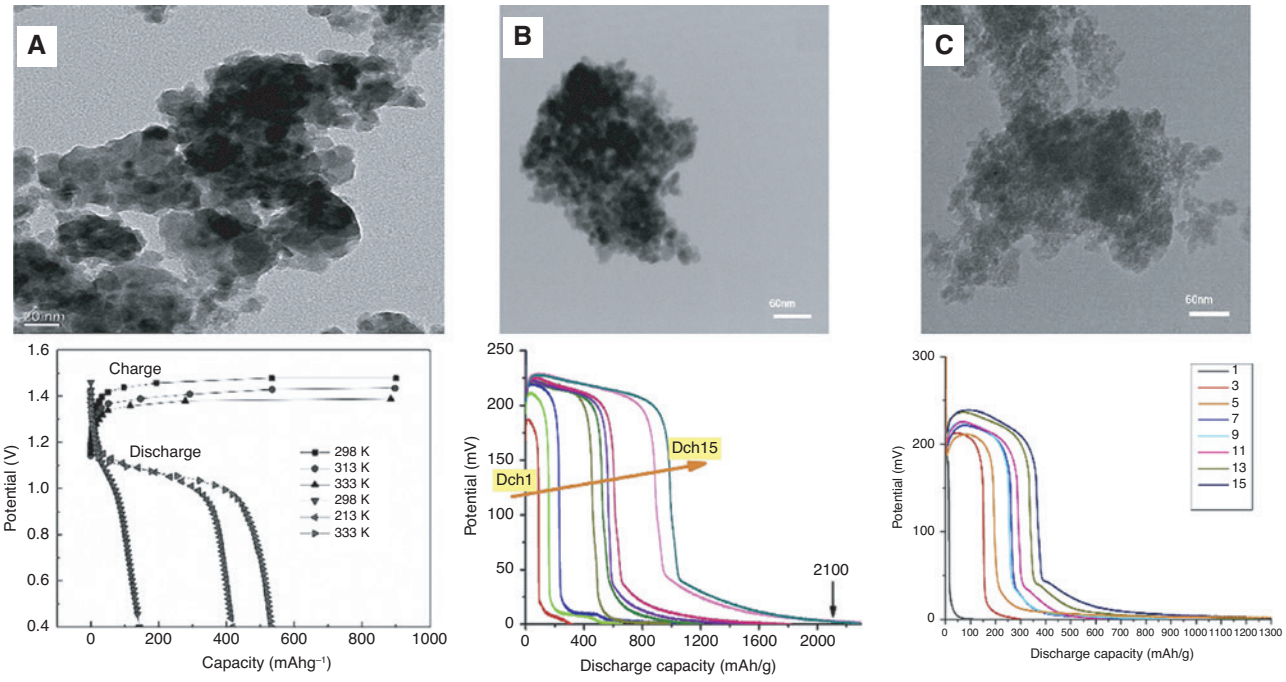

Figure 12: Perovskite nanostructures for H_2 storage and their discharge capacities.
(A) $LaFeO_3$ nanocrystals. Reproduced with permission from [50]. Copyright 2013, American Institute of Physics. (B) $DyFeO_3$ nanocrystals. Reproduced with permission from [277]. Copyright 2018, Elsevier. (C) $Ba_2Co_9O_{14}$ nanocrystals. Reproduced with permission from [278]. Copyright 2019, Elsevier.

of 2100 mA/g after 15 cycles (Figure 12B), which is very high not only among the perovskites but also between other common materials for hydrogen storage [51]. Furthermore, $Ba_2Co_9O_{14}$ nanocrystals of 10–30 nm were studied for the same applications by the same group but the recorded discharge capacity was lower (850 mA/g after 15 cycles) (Figure 12C) than the $DyFeO_3$ nanocrystals. [278]. The proposed mechanism of hydrogen storage lies in a two-step reaction. The first step takes place on the surface of the material over a few atomic layers, while the second occurs inside as the H-atoms are diffused [277]. Although, these studies mentioned that the structural defects may play role in the storage capability, their exact role on the final performance are not yet clear. Also, it would be interesting to study newly solution-processed metal halide nanocrystals in such storage applications.

3 Conclusions and open issues

In recent years the perovskite nanocrystals have been introduced to effectively replace conventional energy materials. The simultaneous need for new energy materials together with the increasing interest for the development of new devices and even exploring new physics, have pushed the research to manipulate the structuring of the perovskite materials at the nanoscale level. The nanostructuring of the perovskites due to their reduced dimensions is advantageous in offering a large surface area, extensive porous structures, controlled transport, and high charge-carrier mobility, strong absorption, and photoluminescence, and confinement effects. In recent year there is a lot of work incorporating them into photovoltaics as active materials or covering the active layer to improve its stability but there has been limited effort to use them as thermoelectric materials or photocatalysts for the CO_2 reduction in solar fuel cells. The utilization of them in CO_2 reduction is a completely new scientific field which has gained increased interest very recently. In addition, perovskite nanocrystals have received considerable attention for energy storage applications due to their excellent catalytic activity, electrical conductivity, and durability. Ion migration through perovskite lattices allows the use of such materials as electrodes for batteries or supercapacitors. Perovskite oxide nanostructures are more investigated for such applications but very recently the metal halides have also shown high specific capacitance and promising stability upon cycling. Finally, the utilization of such nanocrystals in hydrogen storage could be really interesting as hydrogen is the most abundant element on the planet, with the highest energy content amongst all the existing energy sources, but the number

of the perovskite nanocrystals used for such purposes is still limited.

This review article has covered many aspects of the synthesis of nanocrystals made of metal halides or perovskite oxides, but also their applications in energy conversion and storage. Despite the important evolution in the synthesis procedures, there are some open issues which require attention when we use these materials in these applications. Some of these open issues are:

3.1 Synthesis strategies

3.1.1 Surface chemistry and role of the ligands

Despite the huge evolution of synthesis strategies for the fabrication of nanocrystals of different morphologies and chemical phases, there is a poor understanding of the role of the ligands on the nanocrystal quality concerning their stability, carrier transport, but also on the energy device performance in which are included [279]. It is not clear if the ligands passivate structure trap states or introduce new ones and how the crystal defects play a role in the whole reactivity and electronic properties of the passivated nanocrystals.

3.1.2 Stability

Long-term stability issues at ambient conditions or more harsh environments such as high temperature, direct irradiation, light, and humidity have to be carefully addressed when we are interested in industrial applications. The careful choice of a protective ligand has been proposed as an effective way to improve the stability of the nanocrystals but the effect on device performance is something that has to be studied. The encapsulation of the nanocrystals in a matrix or a different material could be another way, but it is still unknown if such shelling could really prevent the nanocrystals from oxygen and moisture [12]. Finally, all-inorganic metal halides or lead-free compounds could effectively improve the stability of the devices, but still the performance of these devices remains very low.

3.1.3 Lead-free compounds

The synthesis of lead-free and environmentally friendly nanocrystals is a demand. Tin- or bismuth-based compounds have been introduced as possible stoichiometries and more recently double perovskites with an elpasolite structure [115]. The synthesis approaches for these perovskite nanocrystals remain limited. Only a few reports exist for elpasolite nanocrystals and all these nanocrystals are of spherical morphology and capped with organic ligands. The performance of bismuth based solar cells remains is very low.

3.1.4 Scale-up synthesis

One of the drawbacks of the synthesis procedures reported in this review is the small quantity of the final product. While there is a huge variety of synthesis procedures for nanocrystals of different morphologies/chemical phases and homogeneous in size and shape, there is still the difficulty of modifying them for large scale production if the purpose is to use these nanocrystals for industrial application. The development of large-scale synthesis procedures which will be cheap and easy is still a real challenge.

3.2 Deposition of nanocrystals in layer form, free of cracks and defects

Perovskite nanocrystals have been used in energy applications due to their large surface area, efficient carrier transport, high absorption coefficient, long-term stability, and tunable bandgap. The morphology and crystallinity are some of the important intrinsic features that affect the final performance of the devices. But in most of the applications these nanocrystals are assembled in films. The shape and size of the nanocrystals and the existence or not of ligands on the surface determine the final structure of the film. The formation of compact and smooth films is a real challenge for such applications. Many methods for the fabrication of films of high quality free of pinholes and cracks have been proposed, but many parameters remain unexplored and have to be controlled. The removal of the capping ligands is a necessity in order to fabricate such films with enhanced electrical properties. For such purposes, various methods for this removal have been proposed, but many times they are insufficient which result in the release of nanocrystals from the surface or cause their undesired growth of the nanocrystals. These affect also the stability of the devices in which are utilized such nanocrystals. The development of new efficient strategies for the effective removal of the capping ligands without affecting their primary structural or morphological features is a requirement.

Accordingly, it is important here to comment on attempts such as the encapsulation of perovskite nanocrystals in perovskite matrices [196] or the incorporation of

nanocrystals between the active layer and the hole transporting layer [17, 18]. Interface engineering is an effective way for obtaining high efficiency and improved stability in the perovskite solar cells through interfacial charge transfer control. In addition, perovskite nanocrystals have been introduced into the absorber layer to reduce charge recombination and improve the charge transfer [203]. This process used to improve the quality of the absorber layer in terms of film structure, morphology, and crystallinity as the nanocrystals behave as nucleation centers in the growth of perovskite films. The high quality of the films leads to improved charge transport and solar cell power conversion efficiency.

References

[1] Kostopoulou A, Kymakis E, Stratakis E. Perovskite nanostructures for photovoltaic and energy storage devices. J Mater Chem A 2018;6:9765–98.

[2] Buller S, Strunk J. Nanostructure in energy conversion. J Energy Chem 2016;25:171–90.

[3] Centi G, Perathoner S. The role of nanostructure in improving the performance of electrodes for energy storage and conversion. Eur J Inorg Chem 2009;26:2851–78.

[4] Zhang W, Eperon GE, Snaith HJ. Metal halide perovskites for energy applications. Nat Energy 2016;1:16048

[5] Tan P, Liu ML, Shao ZP, Ni M. Recent advances in perovskite oxides as electrode materials for nonaqueous lithium-oxygen batteries. Adv Energy Mater 2017;7:1602674.

[6] Zhu L, Liu Y, Su C, Zhou W, Liu ML, Shao ZP. Perovskite $SrCo_{0.9}Nb_{0.1}O_{3\text{-delta}}$ as an anion-intercalated electrode material for supercapacitors with ultrahigh volumetric energy density. Angew Chem Int Edit 2016;55:9576–9.

[7] Zhu L, Ran R, Tade M, Wang W, Shao ZP. Perovskite materials in energy storage and conversion. Asia-Pac J Chem Eng 2016;11:338–69.

[8] Jung HS, Park NG. Perovskite solar cells: from materials to devices. Small 2015;11:10–25.

[9] Pandey R, Vats G, Yun J, Bowen CR, Ho-Baillie AWY, Seidel J. Perovskites for solar and thermal energy harvesting: state of the art technologies, current scenario and future directions. arXiv:1705.05529v1 [cond-mat.mtrl-sci].

[10] Wu H, Zhu X. Perovskite oxide nanocrystals – synthesis, characterization, functionalization, and novel applications, perovskite materials – synthesis, characterisation, properties, and applications, L. Pan, G. Zhu (Eds.), IntechOpen 2016; DOI: 10.5772/61640.

[11] Atta NF, Galal A, El-Ads EH. Perovskite nanomaterials – synthesis, characterization, and applications, perovskite materials – synthesis, characterisation, properties, and applications, L. Pan, G. Zhu (Eds.), IntechOpen 2016; DOI: 10.5772/61280.

[12] Shamsi J, Urban AS, Imran M, De Trizio L, Manna L. Metal halide perovskite nanocrystals: synthesis, post-synthesis modifications, and their optical properties. Chem Rev 2019;119:3296–348.

[13] Wu H, Xia WR, Xue PJ, Zhu XH. Perovskite oxide nanocrystals: synthesis, characterization, physical properties, and applications. Ferroelectrics 2017;518:127–36.

[14] Zhang YP, Liu JY, Wang ZY, et al. Synthesis, properties, and optical applications of low-dimensional perovskites. Chem Commun 2016;52:13637–55.

[15] Swarnkar A, Marshall AR, Sanehira EM, et al. Quantum dot-induced phase stabilization of alpha-$CsPbI_3$ perovskite for high-efficiency photovoltaics. Science 2016;354:92–5.

[16] Akkerman QA, Gandini M, Di Stasio F, et al. Strongly emissive perovskite nanocrystal inks for high-voltage solar cells. Nat Energy 2017;2.

[17] Liu C, Hu M, Zhou X, et al. Efficiency and stability enhancement of perovskite solar cells by introducing $CsPbI_3$ quantum dots as an interface engineering layer. Npg Asia Mater 2018;10:3760–3.

[18] Chen L, Tien C, Tseng Z, Ruan J. Enhanced efficiency of $MAPbI_3$ perovskite solar cells with $FAPbX_3$ perovskite quantum dots. Nanomaterials 2019;9:3760–3.

[19] Zhou DL, Liu DL, Pan GC, et al. Cerium and ytterbium codoped halide perovskite quantum dots: a novel and efficient down-converter for improving the performance of silicon solar cells. Adv Mater 2017;29:1704149.

[20] Liu X, Chueh CC, Zhu ZL, Jo SB, Sun Y, Jen AKY. Highly crystalline Zn_2SnO_4 nanoparticles as efficient electron-transporting layers toward stable inverted and flexible conventional perovskite solar cells. J Mater Chem A 2016;4:15294–301.

[21] Zeng S, Kar P, Thakur UK, Shankar K. A review on photocatalytic CO_2 reduction using perovskite oxide nanomaterials. Nanotechnology 2018;29.

[22] Hou JG, Cao SY, Wu YZ, et al. Inorganic colloidal perovskite quantum dots for robust solar CO_2 reduction. Chem-Eur J 2017;23:9481–5.

[23] Zhou L, Xu YF, Chen BX, Kuang DB, Su CY. Synthesis and photocatalytic application of stable lead-free $Cs_2AgBiBr_6$ perovskite nanocrystals. Small 2018;14.

[24] Xu YF, Yang MZ, Chen BX, et al. A $CsPbBr_3$ perovskite quantum dot/graphene oxide composite for photocatalytic CO_2 reduction. J Am Chem Soc 2017;139:5660–3.

[25] Wang QL, Tao LM, Jiang XX, Wang MK, Shen Y. Graphene oxide wrapped $CH_3NH_3PbBr_3$ perovskite quantum dots hybrid for photoelectrochemical CO_2 reduction in organic solvents. Appl Surf Sci 2019;465:607–13.

[26] Wang MC, Lin SC. Anisotropic and ultralow phonon thermal transport in organic-inorganic hybrid perovskites: atomistic insights into solar cell thermal management and thermoelectric energy conversion efficiency. Adv Funct Mater 2016;26:5297–306.

[27] Wu TJ, Gao P. Development of perovskite-type materials for thermoelectric application. Materials 2018;11:999.

[28] Filippetti A, Caddeo C, Delugas P, Mattoni A. Appealing perspectives of hybrid lead-iodide perovskites as thermoelectric materials. J Phys Chem C 2016;120:28472–9.

[29] Fu ZH, Lin XJ, Huang T, Yu AS. Nano-sized $La_{0.8}Sr_{0.2}MnO_3$ as oxygen reduction catalyst in nonaqueous Li/O_2 batteries. J Solid State Electr 2012;16:1447–52.

[30] Xia HR, Sun WT, Peng LM. Hydrothermal synthesis of organometal halide perovskites for Li-ion batteries. Chem Commun 2015;51:13787–90.

[31] Vicente N, Garcia-Belmonte G. Methylammonium lead bromide perovskite battery anodes reversibly host high Li-Ion concentrations. J Phys Chem Lett 2017;8:1371–4.

[32] Kostopoulou A, Vernardou D, Savva K, Stratakis E. All-inorganic lead halide perovskite nanohexagons for high performance air-stable lithium batteries. Nanoscale 2019;11:882–9.
[33] Lee JJ, Oh MY, Nahm KS. Effect of ball milling on electrocatalytic activity of perovskite $La_{0.6}Sr_{0.4}CoO_{3-\delta}$ applied for lithium air battery. J Electrochem Soc 2016;163:A244–50.
[34] Francia C, Amici J, Tasarkuyu E, Coskun A, Gul OF, Sener T. What do we need for the lithium-air batteries: a promoter or a catalyst? Internat J Hydrogen Energy 2016;41:20583–91.
[35] Zhu HY, Zhang PF, Dai S. Recent advances of lanthanum-based perovskite oxides for catalysis. Acs Catal 2015;5:6370–85.
[36] Sun QM, Gu QL, Zhu KJ, Wang J, Qiu JH. Stabilized temperature-dependent dielectric properties of Dy-doped $BaTiO_3$ ceramics derived from sol-hydrotherrnally synthesized nanopowders. Ceram Int 2016;42:3170–6.
[37] Sunarso J, Torriero AAJ, Zhou W, Howlett PC, Forsyth M. Oxygen reduction reaction activity of La-based perovskite oxides in alkaline medium: a thin-film rotating ring-disk electrode study. J Phys Chem C 2012;116:5827–34.
[38] Liu GX, Chen HB, Xia L, et al. Hierarchical mesoporous/macroporous perovskite $La_{0.5}Sr_{0.5}CoO_{3-x}$ nanotubes: a bifunctional catalyst with enhanced activity and cycle stability for rechargeable lithium oxygen batteries. Acs Appl Mater Inter 2015;7:22478–86.
[39] Xu J-J, Xu D, Wang Z-L, Wang H-G, Zhang L-L, Zhang X-B. Synthesis of perovskite-based porous $La_{0.75}Sr_{0.25}MnO_3$ nanotubes as a highly efficient electrocatalyst for rechargeable lithium-oxygen batteries. Angew Chem 2013;52:3887–90.
[40] Lu FL, Wang YR, Jin C, Li F, Yang RZ, Chen FL. Microporous $La_{0.8}Sr_{0.2}MnO_3$ perovskite nanorods as efficient electrocatalysts for lithium air battery. J Power Sources 2015;293:726–33.
[41] Bu YF, Gwon O, Nam G, et al. A highly efficient and robust cation ordered perovskite oxide as a bifunctional catalyst for rechargeable zinc-air batteries. Acs Nano 2017;11:11594–601.
[42] Luo Y, Lu FL, Jin C, Wang YR, Yang RZ, Yang CH. $NiCo_2O_4$@ $La_{0.8}Sr_{0.2}MnO_3$ core-shell structured nanorods as efficient electrocatalyst for Li-O_2 battery with enhanced performances. J Power Sources 2016;319:19–26.
[43] Park HW, Lee DU, Park MG, et al. Perovskite-nitrogen-doped carbon nanotube composite as bifunctional catalysts for rechargeable lithium-air batteries. Chemsuschem 2015;8:1058–65.
[44] Yoon KR, Kim DS, Ryu WH, et al. Tailored combination of low dimensional catalysts for efficient oxygen reduction and evolution in Li-O_2 batteries. Chemsuschem 2016;9:2080–8.
[45] Zhang XL, Gong YD, Li SQ, Sun CW. Porous Perovskite $La_{0.6}Sr_{0.4}Co_{0.8}Mn_{0.2}O_3$ Nanofibers loaded with RuO_2 nanosheets as an efficient and durable bifunctional catalyst for rechargeable Li-O_2 batteries. Acs Catal 2017;7:7737–47.
[46] Hu J, Liu QN, Shi LN, Shi ZW, Huang H. Silver decorated $LaMnO_3$ nanorod/graphene composite electrocatalysts as reversible metal-air battery electrodes. Appl Surf Sci 2017;402:61–9.
[47] Cao Y, Lin BP, Sun Y, Yang H, Zhang XQ. Symmetric/asymmetric supercapacitor based on the perovskite-type lanthanum cobaltate nanofibers with Sr-substitution. Electrochim Acta 2015;178:398–406.
[48] Shao TY, You HH, Zhai ZJ, Liu TH, Li M, Zhang L. Hollow spherical $LaNiO_3$ supercapacitor electrode synthesized by a facile template-free method. Mater Lett 2017;201:122–4.
[49] Li ZJ, Zhang WY, Wang HY, Yang BC. Two-dimensional perovskite $LaNiO_3$ nanosheets with hierarchical porous structure for high-rate capacitive energy storage. Electrochim Acta 2017;258:561–70.
[50] Wang Q, Deng G, Chen ZQ, Chen YG, Cheng NP. Electrochemical hydrogen property improved in nano-structured perovskite oxide $LaFeO_3$ for Ni/MH battery. J Appl Phys 2013;113:053305.
[51] Kaur M, Pal K. Review on hydrogen storage materials and methods from an electrochemical viewpoint. J Energy Storage 2019;23:234–49.
[52] Yun QB, Lu QP, Zhang X, Tan CL, Zhang H. Three-dimensional architectures constructed from transition-metal dichalcogenide nanomaterials for electrochemical energy storage and conversion. Angew Chem Int Edit 2018;57:626–46.
[53] Choi JW, Wang DH, Wang DW. Nanomaterials for energy conversion and storage. Chemnanomat 2016;2:560–1.
[54] dos Santos MC, Kesler O, Reddy ALM. Nanomaterials for energy conversion and storage. J Nanomater 2012;159249.
[55] Kou TY, Wang GM, Lu XH, Song Y, Zhai T. Functional nanomaterials for energy conversion and storage. J Nanomater 2016;8521320.
[56] Pan LK. Functional semiconductor nanomaterials for renewable energy conversion and storage. Curr Nanosci 2016;12:316.
[57] Zhang QF, Uchaker E, Candelaria SL, Cao GZ. Nanomaterials for energy conversion and storage. Chem Soc Rev 2013;42:3127–71.
[58] Akkerman QA, Park S, Radicchi E, et al. Nearly monodisperse insulator Cs_4PbX_6 (X=Cl, Br, I) nanocrystals, their mixed halide compositions, and their transformation into $cspbx_3$ nanocrystals. Nano Lett 2017;17:1924–30.
[59] Jang DM, Kim DH, Park K, Park J, Lee JW, Song JK. Ultrasound synthesis of lead halide perovskite nanocrystals. J Mater Chem C 2016;4:10625–9.
[60] Chen LJ, Lee CR, Chuang YJ, Wu ZH, Chen CY. Synthesis and optical properties of lead-free cesium tin halide perovskite quantum rods with high-performance solar cell application. J Phys Chem Lett 2016;7:5028–35.
[61] Kostopoulou A, Sygletou M, Brintakis K, Lappas A, Stratakis E. Low-temperature benchtop-synthesis of all-inorganic perovskite nanowires. Nanoscale 2017;9:18202–7.
[62] Hintermayr VA, Richter AF, Ehrat F, et al. Tuning the optical properties of perovskite nanoplatelets through composition and thickness by ligand-assisted exfoliation. Adv Mater 2016;28:9478–85.
[63] Ashiri R, Nemati A, Ghamsari MS, Sanjabi S, Aalipour M. A modified method for barium titanate nanoparticles synthesis. Mater Res Bull 2011;46:2291–5.
[64] O'Brien S, Brus L, Murray CB. Synthesis of monodisperse nanoparticles of barium titanate: toward a generalized strategy of oxide nanoparticle synthesis. J Am Chem Soc 2001;123:12085–6.
[65] Utara S, Hunpratub S. Ultrasonic assisted synthesis of $BaTiO_3$ nanoparticles at 25°C and atmospheric pressure. Ultrason Sonochem 2018;41:441–8.
[66] Caruntu D, Rostamzadeh T, Costanzo T, Parizi SS, Caruntu G. Solvothermal synthesis and controlled self-assembly of monodisperse titanium-based perovskite colloidal nanocrystals. Nanoscale 2015;7:12955–69.
[67] Joshi UA, Lee JS. Template-free hydrothermal synthesis of single-crystalline barium titanate and strontium titanate nanowires. Small 2005;1:1172–6.

[68] Schmidt LC, Pertegas A, Gonzalez-Carrero S, et al. Nontemplate synthesis of $CH_3NH_3PbBr_3$ perovskite nanoparticles. J Am Chem Soc 2014;136:850–3.
[69] Zhang F, Zhong HZ, Chen C, et al. Brightly luminescent and color-tunable colloidal $CH_3NH_3PbX_3$ (X=Br, I, Cl) quantum dots: potential alternatives for display technology. Acs Nano 2015;9:4533–42.
[70] Zhu F, Men L, Guo YJ, et al. Shape evolution and single particle luminescence of organometal halide perovskite nanocrystals. Acs Nano 2015;9:2948–59.
[71] Cho J, Choi YH, O'Loughlin TE, De Jesus L, Banerjee S. Ligand-mediated modulation of layer thicknesses of perovskite methylammonium lead bromide nanoplatelets. Chem Mater 2016;28:6909–16.
[72] Seth S, Samanta A. A Facile methodology for engineering the morphology of $CsPbX_3$ perovskite nanocrystals under ambient condition. Sci Rep-UK 2016;6:37693.
[73] Zhang YH, Saidaminov MI, Dursun I, et al. Zero -dimensional Cs_4PbBr_6 perovskite nanocrystals. J Phys Chem Lett 2017;8:961–5.
[74] Shamsi J, Abdelhady AL, Accornero S, et al. N-Methylformamide as a source of methylammonium ions in the synthesis of lead halide perovskite nanocrystals and bulk crystals. Acs Energy Lett 2016;1:1042–8.
[75] Li XM, Wu Y, Zhang SL, et al. $CsPbX_3$ quantum dots for lighting and displays: room-temperature synthesis, photoluminescence superiorities, underlying origins and white light-emitting diodes. Adv Funct Mater 2016;26:2435–45.
[76] Yang H, Zhang Y, Pan J, Yin J, Bakr OM, Mohammed OF. Room-temperature engineering of all-inorganic perovskite nanocrsytals with different dimensionalities. Chem Mater 2017;29:8978–82.
[77] Aharon S, Etgar L. Two dimensional organometal halide perovskite nanorods with tunable optical properties. Nano Lett 2016;16:3230–5.
[78] Amgar D, Stern A, Rotem D, Porath D, Etgar L. Tunable length and optical properties of $CsPbX_3$ (X=Cl, Br, I) nanowires with a few unit cells. Nano Lett 2017;17:1007–13.
[79] Sichert JA, Tong Y, Mutz N, et al. Quantum size effect in organometal halide perovskite nanoplatelets. Nano Lett 2015;15:6521–7.
[80] Akkerman QA, Motti SG, Kandada ARS, et al. Solution synthesis approach to colloidal cesium lead halide perovskite nanoplatelets with monolayer-level thickness control. J Am Chem Soc 2016;138:1010–6.
[81] Li GP, Wang H, Zhu ZF, et al. Shape and phase evolution from $CsPbBr_3$ perovskite nanocubes to tetragonal $CsPb_2Br_5$ nanosheets with an indirect bandgap. Chem Commun 2016;52:11296–9.
[82] Liang J, Wang CX, Wang YR, et al. All-inorganic perovskite solar cells. J Am Chem Soc 2016;138:15829–32.
[83] Protesescu L, Yakunin S, Bodnarchuk MI, et al. Nanocrystals of cesium lead halide perovskites ($CsPbX_3$, X=Cl, Br, and I): novel optoelectronic materials showing bright emission with wide color gamut. Nano Lett 2015;15:3692–6.
[84] Li GP, Wang H, Zhang T, et al. Solvent-polarity-engineered controllable synthesis of highly fluorescent cesium lead halide perovskite quantum dots and their use in white light-emitting diodes. Adv Funct Mater 2016;26:8478–86.
[85] Liang ZQ, Zhao SL, Xu Z, et al. Shape-controlled synthesis of all-inorganic $CsPbBr_3$ perovskite nanocrystals with bright blue emission. Acs Appl Mater Inter 2016;8:28824–30.
[86] Luo BB, Pu YC, Yang Y, et al. Synthesis, optical properties, and exciton dynamics of organolead bromide perovskite nanocrystals. J Phys Chem C 2015;119:26672–82.
[87] Song JZ, Li JH, Li XM, Xu LM, Dong YH, Zeng HB. Quantum dot light-emitting diodes based on inorganic perovskite cesium lead halides ($CsPbX_3$). Adv Mater 2015;27:7162–7.
[88] Cottingham P, Brutchey RL. Compositionally dependent phase identity of colloidal $CsPbBr_3$-xIx quantum dots. Chem Mater 2016;28:7574–7.
[89] Meyns M, Peralvarez M, Heuer-Jungemann A, et al. Polymer-enhanced stability of inorganic perovskite nanocrystals and their application in color conversion leds. Acs Appl Mater Inter 2016;8:19579–86.
[90] Liu F, Zhang YH, Ding C, et al. Highly luminescent phase-stable CsPbI(3) perovskite quantum dots achieving near 100% absolute photoluminescence quantum yield. ACS Nano 2017;11:10373–83.
[91] Pan AZ, He B, Fan XY, et al. Insight into the ligand-mediated synthesis of colloidal $CsPbBr_3$ perovskite nanocrystals: the role of organic acid, base, and cesium precursors. Acs Nano 2016;10:7943–54.
[92] Ravi VK, Swarnkar A, Chakraborty R, Nag A. Excellent green but less impressive blue luminescence from $CsPbBr_3$ perovskite nanocubes and nanoplatelets. Nanotechnology 2016;27.
[93] Udayabhaskararao T, Kazes M, Houben L, Lin H, Oron D. Nucleation, growth, and structural transformations of perovskite nanocrystals. Chem Mater 2017;29:1302–8.
[94] Zhang DD, Eaton SW, Yu Y, Dou LT, Yang PD. Solution-phase synthesis of cesium lead halide perovskite nanowires. J Am Chem Soc 2015;137:9230–3.
[95] Imran M, Di Stasio F, Dang ZY, et al. Colloidal synthesis of strongly fluorescent $CsPbBr_3$ nanowires with width tunable down to the quantum confinement regime. Chem Mater 2016;28:6450–4.
[96] Zhang DD, Yu Y, Bekenstein Y, Wong AB, Alivisatos AP, Yang PD. Ultrathin colloidal cesium lead halide perovskite nanowires. J Am Chem Soc 2016;138:13155–8.
[97] Lim DH, Ramasamy P, Kwak DH, Lee JS. Solution-phase synthesis of rubidium lead iodide orthorhombic perovskite nanowires. Nanotechnology 2017;28:255601.
[98] Wang CY, Zhang YK, Wang AF, et al. Controlled synthesis of composition tunable formamidinium cesium double cation lead halide perovskite nanowires and nanosheets with improved stability. Chem Mater 2017;29:2157–66.
[99] Bekenstein Y, Koscher BA, Eaton SW, Yang PD, Alivisatos AP. Highly luminescent colloidal nanoplates of perovskite cesium lead halide and their oriented assemblies. J Am Chem Soc 2015;137:16008–11.
[100] Lv LF, Xu YB, Fang HH, et al. Generalized colloidal synthesis of high-quality, two-dimensional cesium lead halide perovskite nanosheets and their applications in photodetectors. Nanoscale 2016;8:13589–96.
[101] Shamsi J, Dang ZY, Bianchini P, et al. Colloidal synthesis of quantum confined single crystal $CsPbBr_3$ nanosheets with lateral size control up to the micrometer range. J Am Chem Soc 2016;138:7240–3.
[102] Li Z-J, Hofman E, Li J, et al. Photoelectrochemically active and environmentally stable $CsPbBr_3/TiO_2$ Core/shell nanocrystals. Adv Funct Mater 2018;28:1704288.

[103] Singh R, Suranagi SR, Yang SJ, Cho K. Enhancing the power conversion efficiency of perovskite solar cells via the controlled growth of perovskite nanowires. Nano Energy 2018;51:192–8.
[104] Chen M, Zou YT, Wu LZ, et al. Solvothermal synthesis of high-quality all-inorganic cesium lead halide perovskite nanocrystals: from nanocube to ultrathin nanowire. Adv Funct Mater 2017;27:1701121.
[105] Amendola V, Fortunati I, Marega C, Abdelhady AL, Saidaminov MI, Bakr OM. High-purity hybrid organolead halide perovskite nanoparticles obtained by pulsed-laser irradiation in liquid. Chemphyschem 2017;18:1047–54.
[106] Rosa-Pardo I, Rando-Brotons M, Pocoví-Martínez S, Galian RE, Pérez Prieto J. Laser ablation of hybrid perovskite bulks into nanoparticles: adamantylammonium halides as ligands and halide sources. Chem Nano Mat 2019;5:358–33.
[107] Tong Y, Bladt E, Ayguler MF, et al. Highly luminescent cesium lead halide perovskite nanocrystals with tunable composition and thickness by ultrasonication. Angew Chem Int Edit 2016;55:13887–92.
[108] Pan Q, Hu HC, Zou YT, et al. Microwave-assisted synthesis of high-quality "all-inorganic" $CsPbX_3$ (X=Cl, Br, I) perovskite nanocrystals and their application in light emitting diodes. J Mater Chem C 2017;5:10947–54.
[109] Liu HW, Wu ZN, Gao H, et al. One-step preparation of cesium lead halide $CsPbX_3$ (X=CI, Br, and I) perovskite nanocrystals by microwave irradiation. Acs Appl Mater Inter 2017;9:42919–27.
[110] Zhang J, Yang Y, Deng H, et al. High quantum yield blue emission from lead free inorganic antimony halide perovskite colloidal quantum dots. Acs Nano 2017;11:9294–302.
[111] Yang B, Chen JS, Hong F, et al. Lead-free, air-stable all-inorganic cesium bismuth halide perovskite nanocrystals. Angew Chem Int Edit 2017;56:12471–5.
[112] Leng MY, Chen ZW, Yang Y, et al. Lead-free, blue emitting bismuth halide perovskite quantum dots. Angew Chem Int Edit 2016;55:15012–6.
[113] Dolzhnikov DS, Wang C, Xu YD, Kanatzidis MG, Weiss EA. Ligand-free, quantum-confined Cs_2SnI_6 perovskite nanocrystals. Chem Mater 2017;29:7901–7.
[114] Jellicoe TC, Richter JM, Glass HFJ, et al. Synthesis and optical properties of lead-free cesium tin halide perovskite nanocrystals. J Am Chem Soc 2016;138:2941–4.
[115] Creutz SE, Crites EN, De Siena MC, Gamelin DR. Colloidal nanocrystals of lead-free double-perovskite (elpasolite) semiconductors: synthesis and anion exchange to access new materials. Nano Lett 2018;18:1118–23.
[116] Leng MY, Yang Y, Zeng K, et al. All-Inorganic bismuth-based perovskite quantum dots with bright blue photoluminescence and excellent stability. Adv Funct Mater 2018;28:1704446.
[117] Frey MH, Payne DA. Synthesis and processing of barium-titanate ceramics from alkoxide solutions and monolithic gels. Chem Mater 1995;7:123–9.
[118] Kavian R, Saidi A. Sol-gel derived $BaTiO_3$ nanopowders. J Alloy Compd 2009;468:528–32.
[119] Cui B, Yu PF, Wang X. Preparation and characterizatioii of $BaTiO_3$ powders and ceramics by sol-gel process using hexanoic and hexanedioic acid as surfactant. Microelectron Eng 2009;86:352–6.
[120] Li W, Xu ZJ, Chu RQ, Fu P, Hao JG. Structure and electrical properties of $BaTiO_3$ prepared by sol-gel process. J Alloy Compd 2009;482:137–40.
[121] Wang PG, Fan CM, Wang YW, Ding GY, Yuan PH. A dual chelating sol-gel synthesis of $BaTiO_3$ nanoparticles with effective photocatalytic activity for removing humic acid from water. Mater Res Bull 2013;48:869–77.
[122] Ramakanth S, Raju KCJ. Charge transfer induced magnetism in sol-gel derived nanocrystalline $BaTiO_3$. Solid State Commun 2014;187:59–63.
[123] Kappadan S, Gebreab TW, Thomas S, Kalarikkal N. Tetragonal $BaTiO_3$ nanoparticles: an efficient photocatalyst for the degradation of organic pollutants. Mat Sci Semicon Proc 2016;51:42–7.
[124] Cernea M, Secu CE, Vasile BS, Secu M. Structural and optical characterization of sol-gel derived Tm-doped $BaTiO_3$ nanopowders and ceramics. Curr Appl Phys 2013;13:137–41.
[125] Xin CR, Zhang J, Liu Y, Zhang QL, Yang H, Cheng D. Polymorphism and dielectric properties of Sc-doped $BaTiO_3$ nanopowders synthesized by sol-gel method. Mater Res Bull 2013;48:2220–6.
[126] Aghayan M, Zak AK, Behdani M, Hashim AM. Sol-gel combustion synthesis of Zr-doped $BaTiO_3$ nanopowders and ceramics: dielectric and ferroelectric studies. Ceram Int 2014;40:16141–6.
[127] Hwang UY, Park HS, Koo KK. Low-temperature synthesis of fully crystallized spherical $BaTiO_3$ particles by the gel-sol method. J Am Ceram Soc 2004;87:2168–74.
[128] Brutchey RL, Morse DE. Template-free, low-temperature synthesis of crystalline barium titanate nanoparticles under bio-inspired conditions. Angew Chem Int Edit 2006;45:6564–6.
[129] Mohammadi MR, Fray DJ. Sol-gel derived nanocrystalline and mesoporous barium strontium titanate prepared at room temperature. Particuology 2011;9:235–42.
[130] Khirade PP, Birajdar SD, Raut AV, Jadhav KM. Multiferroic iron doped $BaTiO_3$ nanoceramics synthesized by sol-gel auto combustion: influence of iron on physical properties. Ceram Int 2016;42:12441–51.
[131] Lombardi J, Pearsall F, Li WL, O'Brien S. Synthesis and dielectric properties of nanocrystalline oxide perovskites, $[KNbO_3](1-x)[BaNi_{0.5}Nb_{0.5}O_{3-delta}](x)$, derived from potassium niobate $KNbO_3$ by gel collection. J Mater Chem C 2016;4:7989–98.
[132] Du ZZ, Yang P, Wang L, et al. Electrocatalytic performances of $LaNi_1$-xMgxO_3 perovskite oxides as bi-functional catalysts for lithium air batteries. J Power Sources 2014;265:91–6.
[133] Liu C, Zou BS, Rondinone AJ, Zhang ZJ. Sol-gel synthesis of free-standing ferroelectric lead zirconate titanate nanoparticles. J Am Chem Soc 2001;123:4344–5.
[134] Lee CY, Tai NH, Sheu HS, Chiu HT, Hsieh SH. The formation of perovskite $PbTiO_3$ powders by sol-gel process. Mater Chem Phys 2006;97:468–71.
[135] Ianculescu AC, Vasilescu CA, Crisan M, et al. Formation mechanism and characteristics of lanthanum-doped $BaTiO_3$ powders and ceramics prepared by the sol-gel process. Mater Charact 2015;106:195–207.
[136] Chandrasekhar SM, Kumar P. Microwave sintered sol-gel derived $BaTiO_3$ and $Ba_{0.95}La_{0.05}TiO_3$ ceramic samples for capacitor applications. Ceram Int 2016;42:10587–92.
[137] Ciftci E, Rahaman MN, Shumsky M. Hydrothermal precipitation and characterization of nanocrystalline $BaTiO_3$ particles. J Mater Sci 2001;36:4875–82.

[138] Zhu KJ, Qiu JH, Kajiyoshi K, Takai M, Yanagisawa K. Effect of washing of barium titanate powders synthesized by hydrothermal method on their sinterability and piezoelectric properties. Ceram Int 2009;35:1947–51.
[139] Hayashi H, Noguchi T, Islam NM, Hakuta Y, Imai Y, Ueno N. Hydrothermal synthesis of $BaTiO_3$ nanoparticles using a supercritical continuous flow reaction system. J Cryst Growth 2010;312:1968–72.
[140] Chen CL, Wei YL, Jiao XL, Chen DR. Hydrothermal synthesis of $BaTiO_3$: crystal phase and the Ba2+ ions leaching behavior in aqueous medium. Mater Chem Phys 2008;110:186–91.
[141] Lee WW, Chung WH, Huang WS, et al. Photocatalytic activity and mechanism of nano-cubic barium titanate prepared by a hydrothermal method. J Taiwan Inst Chem E 2013;44:660–9.
[142] Matsui K, Noguchi T, Islam NM, Hakuta Y, Hayashi H. Rapid synthesis of $BaTiO_3$ nanoparticles in supercritical water by continuous hydrothermal flow reaction system. J Cryst Growth 2008;310:2584–9.
[143] Wei X, Xu G, Ren ZH, Wang YG, Shen G, Han GR. Size-controlled synthesis of $BaTiO_3$ nanocrystals via a hydrothermal route. Mater Lett 2008;62:3666–9.
[144] Garrido-Hernandez A, Garcia-Murillo A, Carrillo-Romo FD, et al. Structural studies of $BaTiO_3$:Er3+ and $BaTiO_3$:Yb3+ powders synthesized by hydrothermal method. J Rare Earth 2014;32:1016–21.
[145] Cao Y, Zhu KJ, Liu JS, Qiu JH. Fabrication of $BaTiO_3$ nanoparticles and its formation mechanism using the high temperature mixing method under hydrothermal conditions. Adv Powder Technol 2014;25:853–8.
[146] Cai W, Rao TK, Wang AW, et al. A simple and controllable hydrothermal route for the synthesis of monodispersed cube-like barium titanate nanocrystals. Ceram Int 2015;41:4514–22.
[147] Zhang J, Zhao YB, Zhao X, Liu ZL, Chen W. Porous perovskite $LaNiO_3$ nanocubes as cathode catalysts for Li-O_2 batteries with low charge potential. Sci Rep-UK 2014;4:6005.
[148] Mao YB, Banerjee S, Wong SS. Hydrothermal synthesis of perovskite nanotubes. Chem Commun 2003:408–9.
[149] Wang YG, Xu G, Yang LL, et al. Hydrothermal synthesis of single-crystal $BaTiO_3$ dendrites. Mater Lett 2009;63:239–41.
[150] Krzmanc MM, Klement D, Jancar B, Suvorov D. Hydrothermal conditions for the formation of tetragonal $BaTiO_3$ particles from potassium titanate and barium salt. Ceram Int 2015;41:15128–37.
[151] Pinceloup P, Courtois C, Vicens J, Leriche A, Thierry B. Evidence of a dissolution-precipitation mechanism in hydrothermal synthesis of barium titanate powders. J Eur Ceram Soc 1999;19:973–7.
[152] Kim DW, Shin SS, Cho IS, et al. Synthesis and photovoltaic property of fine and uniform Zn_2SnO_4 nanoparticles. Nanoscale 2012;4:557–62.
[153] Adireddy S, Lin CK, Cao BB, Zhou WL, Caruntu G. Solution-based growth of monodisperse cube-like $BaTiO_3$ colloidal nanocrystals. Chem Mater 2010;22:1946–8.
[154] Li J, Inukai K, Tsuruta A, Takahashi Y, Shin W. Synthesis of highly disperse tetragonal $BaTiO_3$ nanoparticles with core-shell by a hydrothermal method. J Asian Ceramic Soc 2017;5:444–51.
[155] Chavez E, Fuentes S, Zarate RA, Padilla-Campos L. Structural analysis of nanocrystalline $BaTiO_3$. J Mol Struct 2010;984:131–6.
[156] Zheng HJ, Zhu KJ, Wu QL, Liu JS, Qiu JH. Preparation and characterization of monodispersed $BaTiO_3$ nanocrystals by sol-hydrothemal method. J Cryst Growth 2013;363:300–7.
[157] Wang WW, Cao LX, Liu W, Su G, Zhang WX. Low-temperature synthesis of $BaTiO_3$ powders by the sol-gel-hydrothermal method. Ceram Int 2013;39:7127–34.
[158] Zanfir AV, Voicu G, Jinga SI, Vasile E, Ionita V. Low-temperature synthesis of $BaTiO_3$ nanopowders. Ceram Int 2016;42:1672–8.
[159] Yu D, Jin AM, Zhang QL, Yang H, Hu L, Cheng D. Scandium and gadolinium co-doped $BaTiO_3$ nanoparticles and ceramics prepared by sol-gel-hydrothermal method: facile synthesis, structural characterization and enhancement of electrical properties. Powder Technol 2015;283:433–9.
[160] Yang X, Ren ZH, Xu G, et al. Monodisperse hollow perovskite $BaTiO_3$ nanostructures prepared by a sol gel hydrothermal method. Ceram Int 2014;40:9663–70.
[161] Meng XH, Wang W, Ke H, Rao JC, Zhou Y. Synthesis of potassium sodium niobate nanostructures by hydrothermal combining with the sol-gel method. Mater Sci Eng B-Adv 2016;212:1–6.
[162] Chen P, Zhang YT, Zhao FQ, Gao HX, Chen XB, An ZW. Facile microwave synthesis and photocatalytic activity of monodispersed $BaTiO_3$ nanocuboids. Mater Charact 2016;114:243–53.
[163] Niederberger M, Garnweitner G, Pinna N, Antonietti M. Nonaqueous and halide-free route to Crystalline $BaTiO_3$, $SrTiO_3$, and (Ba,Sr)TiO_3 nanoparticles via a mechanism involving C-C bond formation. J Am Chem Soc 2004;126:9120–6.
[164] Niederberger M, Pinna N, Polleux J, Antonietti M. A general soft-chemistry route to perovskites and related materials: synthesis of BaTiO(3), BaZrO(3), and LiNbO(3) nanoparticles. Angew Chem Int Edit 2004;43:2270–3.
[165] Mao YP, Mao SY, Ye ZG, Xie ZX, Zheng LS. Solvothermal synthesis and Curie temperature of monodispersed barium titanate nanoparticles. Mater Chem Phys 2010;124:1232–8.
[166] Mohanty D, Chaubey GS, Yourdkhani A, Adireddy S, Caruntu G, Wiley JB. Synthesis and piezoelectric response of cubic and spherical $LiNbO_3$ nanocrystals. Rsc Adv 2012;2:1913–6.
[167] Ji BT, Chen DR, Jiao XL, Zhao ZQ, Jiao YX. Preparation and electrical properties of nanoporous $BaTiO_3$. Mater Lett 2010;64:1836–8.
[168] Yu JC, Zhang LZ, Li Q, Kwong KW, Xu AW, Lin J. Sonochemical preparation of nanoporous composites of titanium oxide and size-tunable strontium titanate crystals. Langmuir 2003;19:7673–5.
[169] Dang F, Kato K, Imai H, Wada S, Haneda H, Kuwabara M. A new effect of ultrasonication on the formation of $BaTiO_3$ nanoparticles. Ultrason Sonochem 2010;17:310–4.
[170] Moghtada A, Ashiri R. Nanocrystals of $XTiO_3$ (X=Ba, Sr, Ni, Ba_xTi_{1-x}) materials obtained through a rapid one-step methodology at 50°C. Ultrason Sonochem 2015;26:293–304.
[171] Dutta DP, Jayakumar OD, Tyagi AK, Girija KG, Pillai CGS, Sharma G. Effect of doping on the morphology and multiferroic properties of $BiFeO_3$ nanorods. Nanoscale 2010;2:1149–54.
[172] Dang F, Kato K, Imai H, Wada S, Haneda H, Kuwabara M. Growth of $BaTiO_3$ nanoparticles in ethanol-water mixture solvent under an ultrasound-assisted synthesis. Chem Eng J 2011;170:333–7.
[173] Wang KH, Wu L, Li L, Yao HB, Qian HS, Yu SH. Large-scale synthesis of highly luminescent perovskite-related $CsPb_2Br_5$ nanoplatelets and their fast anion exchange. Angew Chem Int Edit 2016;55:8328–32.

[174] Kirakosyan A, Kim J, Lee SW, Swathi I, Yoon SG, Choio J. Optical properties of colloidal $CH_3NH_3PbBr_3$ nanocrystals by controlled growth of lateral dimension. Cryst Growth Des 2017;17:794–9.
[175] Ubaldini A, Buscaglia V, Uliana C, Costa G, Ferretti M. Kinetics and mechanism of formation of barium zirconate from barium carbonate and zirconia powders. J Am Ceram Soc 2003;86:19–25.
[176] Li F, Yu XH, Chen LY, Pan HJ, Xin XQ. Solid-state synthesis of $LaCoO_3$ perovskite nanocrystals. J Am Ceram Soc 2002;85:2177–80.
[177] Velchuri R, Kumar BV, Devi VR, Prasad G, Vithal M. Solid state metathesis synthesis of $BaTiO_3$, $PbTiO_3$, $K_{0.5}Bi_{0.5}TiO_3$ and $Na_{0.5}Bi_{0.5}TiO_3$. Ceram Int 2010;36:1485–9.
[178] Mao YB, Banerjee S, Wong SS. Large-scale synthesis of single-crystal line perovskite nanostructures. J Am Chem Soc 2003;125:15718–9.
[179] Chen J, Xing XR, Watson A, et al. Rapid synthesis of multiferroic $BiFeO_3$ single-crystalline nanostructures. Chem Mater 2007;19:3598–600.
[180] He XB, Gao LA. Synthesis of pure phase $BiFeO_3$ powders in molten alkali metal nitrates. Ceram Int 2009;35:975–8.
[181] Zhu XH, Zhou J, Jiang MC, et al. Molten salt synthesis of bismuth ferrite nano- and microcrystals and their structural characterization. J Am Ceram Soc 2014;97:2223–32.
[182] Zhang Y, Wang LQ, Xue DF. Molten salt route of well dispersive barium titanate nanoparticles. Powder Technol 2012;217:629–33.
[183] Li HL, Du ZN, Wang GL, Zhang YC. Low temperature molten salt synthesis of $SrTiO_3$ submicron crystallites and nanocrystals in the eutectic NaCl-KCl. Mater Lett 2010;64:431–4.
[184] Yang J, Li RS, Li XC, Long YL, Zhou JY, Zhang YM. Molten salt synthesis of $SrFeO_3$ nanocrystals. J Ceram Soc Jpn 2011;119:736–9.
[185] Deng H, Qiu YC, Yang SH. General surfactant-free synthesis of $MTiO_3$ (M=Ba, Sr, Pb) perovskite nanostrips. J Mater Chem 2009;19:976–82.
[186] Wang D, Chu XF, Gong ML. Single-crystalline $LaFeO_3$ nanotubes with rough tube walls: synthesis and gas-sensing properties. Nanotechnology 2006;17:5501–5.
[187] Li BR, Shang W, Hu ZL, Zhang NQ. Template-free fabrication of pure single-crystalline $BaTiO_3$ nano-wires by molten salt synthesis technique. Ceram Int 2014;40:73–80.
[188] Zhao H, Yang G, Wang ZY, Cao XW, Gu L, Zhao NJ. Molten salt route of single crystal barium titanate nanowires. J Exp Nanosci 2015;10:1126–36.
[189] Su S, Zuo RZ, Lv DY, Fu J. Synthesis and characterization of (001) oriented $BaTiO_3$ platelets through a topochemical conversion. Powder Technol 2012;217:11–5.
[190] Attar AS, Sichani ES, Sharafi S. Structural and dielectric properties of Bi-doped barium strontium titanate nanopowders synthesized by sol-gel method. J Mater Res Technol 2017;6:108–15.
[191] Im JH, Lee CR, Lee JW, Park SW, Park NG. 6.5% efficient perovskite quantum-dot-sensitized solar cell. Nanoscale 2011;3:4088–93.
[192] Im JH, Chung J, Kim SJ, Park NG. Synthesis, structure, and photovoltaic property of a nanocrystalline 2H perovskite-type novel sensitizer $(CH_3CH_2NH_3)PbI_3$. Nanoscale Res Lett 2012;7:353.
[193] Zhao YX, Zhu K. Efficient planar perovskite solar cells based on 1.8 eV band gap $CH_3NH_3PbI_2Br$ nanosheets via thermal decomposition. J Am Chem Soc 2014;136:12241–4.
[194] Im JH, Luo JS, Franckevicius M, et al. Nanowire perovskite solar cell. Nano Lett 2015;15:2120–6.
[195] Hoffman JB, Zaiats G, Wappes I, Kamat PV. $CsPbBr_3$ solar cells: controlled film growth through layer-by-layer quantum dot deposition. Chem Mater 2017;29:9767–74.
[196] Zhan XS, Jin ZW, Zhan JR, et al. All-ambient processed binary $CsPbBr_3$-$CsPb_2Br_5$ perovskites with synergistic enhancement for high-efficiency Cs-Pb-Br-based solar cells. Acs Appl Mater Inter 2018;10:7145–54.
[197] Ghosh D, Ali MY, Chaudhary DK, Bhattacharyya S. Dependence of halide composition on the stability of highly efficient all-inorganic cesium lead halide perovskite quantum dot solar cells. Sol Energ Mat Sol C 2018;185:28–35.
[198] Christodoulou S, Di Stasio F, Pradhan S, Stavrinadis A, Konstantatos G. High-open-circuit-voltage solar cells based on bright mixed-halide $CsPbBrI_2$ perovskite nanocrystals synthesized under ambient air conditions. J Phys Chem C 2018;122:7621–6.
[199] Panigrahi S, Jana S, Calmeiro T, Nunes D, Martins R, Fortunato E. Imaging the anomalous charge distribution inside $CsPbBr_3$ perovskite quantum dots sensitized solar cells. ACS Nano 2017;11:10214–21.
[200] Liu F, Ding C, Zhang Y, et al. GeI_2 additive for high optoelectronic quality $CsPbI_3$ quantum dots and their application in photovoltaic devices. Chem Mater 2019;31:798–807.
[201] Liao JF, Li WG, Rao HS, et al. Inorganic cesium lead halide $CsPbX_3$ nanowires for long-term stable solar cells. Sci China Mater 2017;60:285–94.
[202] Sanehira EM, Marshall AR, Christians JA, et al. Enhanced mobility $CsPbI_3$ quantum dot arrays for record-efficiency, high-voltage photovoltaic cells. Sci Adv 2017;3:eaao4204.
[203] Gao Y, Wu Y, Lu H, et al. $CsPbBr_3$ perovskite nanoparticles as additive for environmentally stable perovskite solar cells with 20.46% efficiency. Nano Energy 2019;59:517–26.
[204] Hazarika A, Zhao Q, Gaulding EA, et al. Perovskite quantum dot photovoltaic materials beyond the reach of thin films: full-range tuning of A-site cation composition. Acs Nano 2018;12:10327–37.
[205] Xu HZ, Yuan HW, Duan JL, Zhao YY, Jiao ZB, Tang QW. Lead-free $CH_3NH_3SnBr_3$-xIx perovskite quantum dots for mesoscopic solar cell applications. Electrochim Acta 2018;282:807–12.
[206] Bai F, Hu YH, Hu YQ, Qiu T, Miao XL, Zhang SF. Lead-free, air-stable ultrathin $Cs_3Bi_2I_9$ perovskite nanosheets for solar cells. Sol Energ Mat Sol C 2018;184:15–21.
[207] Poli I, Liang X, Baker R, Eslava S, Cameron PJ. Enhancing the hydrophobicity of perovskite solar cells using C18 capped $CH_3NH_3PbI_3$ nanocrystals. J Mater Chem C 2018;6:7149–56.
[208] Zhang ZL, Chen ZH, Zhang JB, et al. Significant Improvement in the performance of PbSe quantum dot solar cell by introducing a $CsPbBr_3$ perovskite colloidal nanocrystal back layer. Adv Energy Mater 2017;7:1601773.
[209] Yang ZY, Janmohamed A, Lan XZ, et al. Colloidal quantum dot photovoltaics enhanced by perovskite shelling. Nano Lett 2015;15:7539–43.

[210] Kirmani AR, de Arguer FPG, Fan JZ, et al. Molecular doping of the hole-transporting layer for efficient, single-step-deposited colloidal quantum dot photovoltaics. Acs Energy Lett 2017;2:1952–9.
[211] Zhang X, Zhang J, Phuyal D, et al. Inorganic $CsPbI_3$ perovskite coating on PbS quantum dot for highly efficient and stable infrared light converting solar cells. Adv Energy Mater 2018;8:1702049.
[212] Kojima A, Teshima K, Shirai Y, Miyasaka T. Organometal halide perovskites as visible-light sensitizers for photovoltaic cells. J Am Chem Soc 2009;131:6050–6051.
[213] Duan JL, Zhao YY, He BL, Jiao ZB, Tang QW. Controllable synthesis of organic-inorganic hybrid halide perovskite quantum dots for quasi-solid-state solar cells. Electrochim Acta 2018;282:263–9.
[214] Wang YS, Xia ZH, Liu LJ, et al. The light-induced field-effect solar cell concept–perovskite nanoparticle coating introduces polarization enhancing silicon cell efficiency. Adv Mater 2017;29:1606370.
[215] Shin SS, Yang WS, Noh JH, et al. High-performance flexible perovskite solar cells exploiting Zn_2SnO_4 prepared in solution below 100 degrees C. Nat Commun 2015;6:7410.
[216] Kim DW, Shin SS, Lee S, et al. $BaSnO_3$ Perovskite nanoparticles for high efficiency dye-sensitized solar cells. Chemsuschem 2013;6:449–54.
[217] Xu YF, Yang MZ, Chen HY, Liao JF, Wang XD, Kuang DB. Enhanced solar-driven gaseous CO_2 conversion by $CsPbBr_3$ nanocrystal/Pd nanosheet Schottky-junction photocatalyst. ACS Appl Energ Mater 2018;1:5083–9.
[218] Xu YF, Wang XD, Liao JF, Chen BX, Chen HY, Kuang DB. Amorphous-TiO_2-encapsulated $CsPbBr_3$ nanocrystal composite photocatalyst with enhanced charge separation and CO_2 fixation. Adv Mater Interfaces 2018;5:1801015.
[219] Fresno F, Jana P, Renones P, Coronado JM, Serrano DP, O'Shea VAD. CO_2 reduction over $NaNbO_3$ and $NaTaO_3$ perovskite photocatalysts. Photoch Photobio Sci 2017;16:17–23.
[220] Li P, Ouyang SX, Xi GC, Kako T, Ye JH. The effects of crystal structure and electronic structure on photocatalytic H-2 evolution and CO_2 reduction over two phases of perovskite-structured $NaNbO_3$. J Phys Chem C 2012;116:7621–8.
[221] Shi HF, Chen GQ, Zhang CL, Zou ZG. Polymeric g-C_3N_4 coupled with $NaNbO_3$ nanowires toward enhanced photocatalytic reduction of CO_2 into renewable fuel. Acs Catal 2014;4:3637–43.
[222] Shi HF, Zou ZG. Photophysical and photocatalytic properties of ANbO(3) (A=Na, K) photocatalysts. J Phys Chem Solids 2012;73:788–92.
[223] Zhou Y, Tian ZP, Zhao ZY, et al. High-yield synthesis of ultrathin and uniform Bi_2WO_6 square nanoplates benefitting from photocatalytic reduction of CO_2 into renewable hydrocarbon fuel under visible light. Acs Appl Mater Inter 2011;3:3594–601.
[224] Sun ZX, Yang ZM, Liu HF, Wang HQ, Wu ZB. Visible-light CO_2 photocatalytic reduction performance of ball-flower-like Bi_2WO_6 synthesized without organic precursor: effect of post-calcination and water vapor. Appl Surf Sci 2014;315:360–7.
[225] Wang M, Han QT, Li L, et al. Construction of an all-solid-state artificial Z-scheme system consisting of Bi_2WO_6/Au/CdS nanostructure for photocatalytic CO_2 reduction into renewable hydrocarbon fuel. Nanotechnology 2017;28:1–8.
[226] Cowen LM, Atoyo J, Carnie MJ, Baran D, Schroeder BC. Review – organic materials for thermoelectric energy generation. Ecs J Solid State Sc 2017;6:N3080–8.
[227] Forman C, Muritala IK, Pardemann R, Meyer B. Estimating the global waste heat potential. Renew Sust Energ Rev 2016;57:1568–79.
[228] Biswas K, He JQ, Blum ID, et al. High-performance bulk thermoelectrics with all-scale hierarchical architectures. Nature 2012;489:414–18.
[229] Bell LE. Cooling, heating, generating power, and recovering waste heat with thermoelectric systems. Science 2008;321:1457–61.
[230] DiSalvo FJ. Thermoelectric cooling and power generation. Science 1999;285:703–6.
[231] Bubnova O, Crispin X. Towards polymer-based organic thermoelectric generators. Energ Environ Sci 2012;5:9345–62.
[232] LeBlanc S. Thermoelectric generators: linking material properties and systems engineering for waste heat recovery applications. Sustain Mater Technolog 2014;1–2:26–35.
[233] Majumdar A. Thermoelectricity in semiconductor nanostructures. Science 2004;303:777–8.
[234] He YP, Galli G. Perovskites for solar thermoelectric applications: a first principle study of $CH_3NH_3Al_3$ (A=Pb and Sn). Chem Mater 2014;26:5394–400.
[235] Dresselhaus MS, Chen G, Tang MY, et al. New directions for low-dimensional thermoelectric materials. Adv Mater 2007;19:1043–53.
[236] Shim W, Ham J, Lee KI, Jeung WY, Johnson M, Lee W. On-film formation of Bi nanowires with extraordinary electron mobility. Nano Lett 2009;9:18–22.
[237] Hao F, Stoumpos CC, Cao DH, Chang RPH, Kanatzidis MG. Lead-free solid-state organic-inorganic halide perovskite solar cells. Nat Photonics 2014;8:489–94.
[238] Stoumpos CC, Malliakas CD, Kanatzidis MG. Semiconducting tin and lead iodide perovskites with organic cations: phase transitions, high mobilities, and near-infrared photoluminescent properties. Inorg Chem 2013;52:9019–38.
[239] Takahashi Y, Hasegawa H, Takahashi Y, Inabe T. Hall mobility in tin iodide perovskite $CH_3NH_3SnI_3$: evidence for a doped semiconductor. J Solid State Chem 2013;205:39–43.
[240] Mettan X, Pisoni R, Matus P, et al. Tuning of the thermoelectric figure of merit of $CH_3NH_3MI_3$ (M=Pb,Sn) photovoltaic perovskites. J Phys Chem C 2015;119:11506–10.
[241] Kabir R, Zhang TS, Wang DY, et al. Improvement in the thermoelectric properties of $CaMnO_3$ perovskites by W doping. J Mater Sci 2014;49:7522–8.
[242] Tathavadekar M, Krishnamurthy S, Banerjee A, et al. Low-dimensional hybrid perovskites as high performance anodes for alkali-ion batteries. J Mater Chem A 2017;5:18634–42.
[243] Dawson JA, Naylor AJ, Eames C, et al. Mechanisms of lithium intercalation and conversion processes in organic-inorganic halide perovskites. Acs Energy Lett 2017;2:1818–24.
[244] Wu J, Li X, Zhao Y, et al. Interface engineering in solid state Li metal batteries by quasi-2D hybrid perovskites. J Mater Chem A 2018;6:20896.
[245] Ramirez D, Suto Y, Rosero-Navarro NC, Miura A, Tadanaga K, Jaramillo F. Structural and electrochemical evaluation of three- and two- dimensional organohalide perovskites and their influence on the reversibility of lithium intercalation. Inorg Chem 2018;57:4181–8.

[246] Sun N, Liu HX, Yu ZY, Zheng ZN, Shao CY. The $La_{0.6}Sr_{0.4}CoO_3$ perovskite catalyst for Li-O-2 battery. Solid State Ionics 2014;268:125–30.
[247] Jin C, Yang Z, Cao X, Lu F, Yang R. A novel bifunctional catalyst of $Ba_{0.9}Co_{0.5}Fe_{0.4}Nb_{0.1}O_{3-\delta}$ perovskite for lithium-air battery. Internat J Hydrogen Energy 2014;39:2526–30.
[248] Xu Q, Han XP, Ding F, et al. A highly efficient electrocatalyst of perovskite $LaNiO_3$ for nonaqueous Li-O_2 batteries with superior cycle stability. J Alloy Compd 2016;664:750–5.
[249] Kalubarme RS, Park GE, Jung KN, Shin KH, Ryu WH, Park CJ. $LaNixCo_{1-x}O_{3-delta}$ perovskites as catalyst material for non-aqueous lithium-oxygen batteries. J Electrochem Soc 2014;161:A880–9.
[250] Chen CF, King G, Dickerson RM, et al. Oxygen-deficient $BaTiO_{3-x}$ perovskite as an efficient bifunctional oxygen electrocatalyst. Nano Energy 2015;13:423–32.
[251] Cheng JF, Zhang M, Jiang YX, et al. Perovskite $La_{0.6}Sr_{0.4}Co_{0.2}Fe_{0.8}O_3$ as an effective electrocatalyst for non-aqueous lithium air batteries. Electrochim Acta 2016;191:106–15.
[252] Wang ZD, You Y, Yuan J, et al. Nickel-Doped $La_{0.8}Sr_{0.2}Mn_{1-x}NixO_3$ nanoparticles containing abundant oxygen vacancies as an optimized bifunctional catalyst for oxygen cathode in rechargeable lithium-air batteries. Acs Appl Mater Inter 2016;8:6520–8.
[253] Lim C, Kim C, Gwon O, et al. Nano-perovskite oxide prepared via inverse microemulsion mediated synthesis for catalyst of lithium-air batteries. Electrochim Acta 2018;275:248–55.
[254] Li PF, Zhang JK, Yu QL, et al. One-dimensional porous $La_{0.5}Sr_{0.5}CoO_{2.91}$ nanotubes as a highly efficient electrocatalyst for rechargeable lithium-oxygen batteries. Electrochim Acta 2015;165:78–84.
[255] He KQ, Zha JW, Du P, et al. Tailored high cycling performance in a solid polymer electrolyte with perovskite-type $Li_{0.33}La_{0.557}TiO_3$ nanofibers for all-solid-state lithium ion batteries. Dalton T 2019;48:3263–9.
[256] Gong H, Wang T, Guo H, et al. Fabrication of perovskite-based porous nanotubes as efficient bifunctional catalyst and application in hybrid lithium-oxygen batteries. J Mater Chem A 2018;6:16943–9.
[257] Poonam, Sharma K, Arora A, Tripathi SK. Review of supercapacitors: materials and devices. J Energy Storage 2019;21:801–25.
[258] Mefford JT, Hardin WG, Dai S, Johnston KP, Stevenson KJ. Anion charge storage through oxygen intercalation in $LaMnO_3$ perovskite pseudocapacitor electrodes. Nat Mater 2014;13:726–32.
[259] Shafi PM, Joseph N, Thirumurugan A, Bose AC. Enhanced electrochemical performances of agglomeration-free $LaMnO_3$ perovskite nanoparticles and achieving high energy and power densities with symmetric supercapacitor design. Chem Eng J 2018;338:147–56.
[260] Arjun N, Pan G-T, Yang TCK. The exploration of Lanthanum based perovskites and their complementary electrolytes for the supercapacitor applications. Results in Physics 2017;7:920–6.
[261] Che W, Wei M, Sang Z, Ou Y, Liu Y, Liu J. Perovskite $LaNiO_{3-\delta}$ oxide as an anion-intercalated pseudocapacitor electrode. J Alloy Compd 2018;731:381–8.
[262] Nagamuthu S, Vijayakumar S, Ryu K-S. Cerium oxide mixed $LaMnO_3$ nanoparticles as the negative electrode for aqueous asymmetric supercapacitor devices. Mater Chem Phys 2017;199:543–51.
[263] Elsiddig ZA, Wang D, Xu H, et al. Three-dimensional nitrogen-doped graphene wrapped $LaMnO_3$ nanocomposites as high-performance supercapacitor electrodes. J Alloy Compd 2018;740:148–55.
[264] Lang XQ, Zhang HF, Xue X, et al. Rational design of $La_{0.85}Sr_{0.15}MnO_3$@$NiCo_2O_4$ core-shell architecture supported on Ni foam for high performance supercapacitors. J Power Sources 2018;402:213–20.
[265] Shi W, Ding R, Li X, et al. Bimetallic Co-Mn perovskite fluorides as highly-stable electrode materials for supercapacitors. Chemistry–A Eur J 2017;23:15305–11.
[266] Ding R, Li X, Shi W, et al. Perovskite $KNi_{0.8}/Co_{0.2}/F_3$ nanocrystals for supercapacitors. J Mater Chem A 2017;5:17822–7.
[267] Lokhande CD, Gujar TP, Shinde VR, Mane RS, Han S-H. Electrochemical supercapacitor application of pervoskite thin films. Electrochem Commun 2007;9:1805–9.
[268] Yin S, Wu Y, Chen J, et al. Facile hydrothermal synthesis of $BiFeO_3$ nanoplates for enhanced supercapacitor properties. Funct Mater Lett 2018;11:1850013.
[269] Alam M, Karmakar K, Pal M, Mandal K. Electrochemical supercapacitor based on double perovskite Y_2NiMnO_6 nanowires. Rsc Adv 2016;6:114722–6.
[270] Rai A, Thakur AK. Effect of Na and Mn substitution in perovskite type $LaFeO_3$ for storage device applications. Ionics 2017;23:2863–9.
[271] George G, Jackson SL, Luo CQ, et al. Effect of doping on the performance of high-crystalline $SrMnO_3$ perovskite nanofibers as a supercapacitor electrode. Ceram Int 2018;44:21982–92.
[272] Songwattanasin P, Karaphun A, Hunpratub S, Maensiri S, Swatsitang E, Amornkitbamrung V. Influence of annealing on microstructure, electrochemical, and magnetic properties of Co-doped $SrTiO_3$ nanocubes. J Superconductivity Novel Magnetism 2019.
[273] Galal A, Hassan HK, Atta NF, Jacob T. Energy and cost-efficient nano-Ru-based perovskites/RGO composites for application in high performance supercapacitors. J Colloid Interf Sci 2019;538:578–86.
[274] Esaka T, Sakaguchi H, Kobayashi S. Hydrogen storage in proton-conductive perovskite-type oxides and their application to nickel-hydrogen batteries. Solid State Ionics 2004;166:351–7.
[275] Deng G, Chen YG, Tao MD, et al. Electrochemical properties and hydrogen storage mechanism of perovskite-type oxide $LaFeO_3$ as a negative electrode for Ni/MH batteries. Electrochim Acta 2010;55:1120–4.
[276] Deng G, Chen YG, Tao MD, et al. Study of the electrochemical hydrogen storage properties of the proton-conductive perovskite-type oxide $LaCrO_3$ as negative electrode for Ni/MH batteries. Electrochim Acta 2010;55:884–6.
[277] Salehabadi A, Salavati-Niasari M, Gholami T, Khoobi A. $Dy_3Fe_5O_{12}$ and $DyFeO_3$ nanostructures: green and facial autocombustion synthesis, characterization and comparative study on electrochemical hydrogen storage. Internat J Hydrogen Energy 2018;43:9713–21.
[278] Razavi FS, Morassaei MS, Salehabadi A, Ghiyasiyan-Arani M, Salavati-Niasari M. Structural characterization and electrochemical hydrogen sorption performances of the polycrystalline $Ba_2Co_9O_{14}$ nanostructures. J Alloy Compd 2019;777:252–8.
[279] Heuer-Jungemann A, Feliu N, Bakaimi I, et al. The role of ligands in the chemical synthesis and applications of inorganic nanoparticles. Chem Rev 2019;119:4819–80.

Bionotes

Athanasia Kostopoulou
Institute of Electronic Structure and Laser (IESL), Foundation for Research and Technology Hellas (FORTH), P.O. Box 1385, Heraklion 70013, Crete, Greece
akosto@iesl.forth.gr

Athanasia Kostopoulou received her BSc degree in Physics (2004) and her MSc degree (2006) in Materials Physics and Technology from the Physics Department at the Aristotle University of Thessaloniki. In 2012, she received her PhD from the Department of Chemistry at the University of Crete, and since then she was a Postdoctoral Fellow in the Institute of Electronic Structure and Laser at FORTH in Heraklion. Since 2016, she has been a part of the group of the Ultrafast Laser Micro and Nano Processing (ULMNP) Laboratory and she is working on the chemical synthesis and elucidation of the microscopic physical or photoinduced mechanisms involving nanocrystal systems. Recently she has been the coordinator of a project funded from the Hellenic Foundation for Research and Innovation (HFRI) and the General Secretariat for Research and Technology (GSRT) related to perovskite nanomaterials for photovoltaic applications.

Konstantinos Brintakis
Institute of Electronic Structure and Laser (IESL), Foundation for Research and Technology Hellas (FORTH), P.O. Box 1385, Heraklion 70013, Crete, Greece

Konstantinos Brintakis is a postdoctoral researcher at IESL-FORTH. He received his BSc in Physics from the Aristotle University of Thessaloniki (AUTh, Greece). He then continued his studies in "Materials Physics and Technology" obtaining his MSc from the Physics Department, AUTh. In 2017, he graduated with a PhD from the same Department and University with "Excellence". His PhD thesis was a collaboration with the Physics Department and the Institute of Electronic Structure and Laser, studying the growth and organization of hybrid nanocrystals and specifically their structural, electronic and magnetic properties. Joining the Ultrafast Laser Micro- and Nano-Processing Group, he is interested in the interaction of matter with lasers and the development of nanostructures in solutions or/and on substrates with physicochemical and laser-assisted approaches. He is currently working on the synthesis and characterization of perovskite nanostructures for energy and gas sensing applications. He is a highly skilled scientist on the characterization of structural and morphological properties with high resolution transmission electron microscopy (HRTEM) and scanning electron microscopy (SEM) microscopy of the developed materials. He is also interested in the exploitation of the produced nanostructures in useful applications.

Nektarios K. Nasikas
Hellenic Foundation for Research and Innovation (HFRI), 127 Vass. Sofias Ave., 11521, Athens, Greece

Nektarios K. Nasikas is a physicist with a PhD in the field of Physical Chemistry of Materials. Over the years he has worked in prestigious research centers and universities, in Greece as well as in the USA, such as the Foundation for Research and Technology Hellas/Institute of Chemical Engineering Sciences (FORTH/ICEHT), the National Hellenic Research Foundation/Theoretical and Physical Chemistry Institute (NHRF/TPCI) and the Peter A. Rock Thermochemistry Laboratory/University of California at Davis. His research interests include novel materials synthesis, materials thermodynamics, novel experimental setup, and design with the use of strong lasers, as well as technology and applications of novel materials possessing special characteristics. He has authored several scientific papers in international scientific journals of high impact such as *Chemistry of Materials*, *Advanced Functional Materials*, *Journal of the American Ceramic Society*, etc. He currently serves as the Director of the Hellenic Foundation for Research and Innovation (HFRI), in Athens, Greece.

Emmanuel Stratakis
Institute of Electronic Structure and Laser (IESL), Foundation for Research and Technology Hellas (FORTH), P.O. Box 1385, Heraklion 70013, Crete, Greece; and University of Crete, Department of Physics, 710 03 Heraklion, Crete, Greece,
stratak@iesl.forth.gr.
https://orcid.org/0000-0002-1908-8618

Dr Emmanuel Stratakis is a Research Director at the Institute of Electronic structure and laser (IESL) (www.iesl.forth.gr) of the Foundation for Research and Technology—Hellas (FORTH) (www.forth.gr). He received his Ph.D. in Physics from the University of Crete in 2001 from the Physics Department, University of Crete. After graduating, he joined as a visiting Researcher the IESL-FORTH working on the ultrafast laser engineering of materials and as an Adjunct Professor at the Department of Materials Science and Technology, University of Crete. In the fall semesters of 2006 and 2008 he was appointed as a visiting Researcher at the Department of Mechanical Engineering of the University of California, Berkeley. In 2007 he was elected Researcher at IESL-FORTH where he is leading the "Ultrafast Laser Micro- and Nano-processing" laboratory (http://stratakislab.iesl.forth.gr; https://www.iesl.forth.gr/en/research/ULNMP-Group). His research interests are in the fields of ultrafast laser interactions with materials for (a) biomimetic micro- and nano-structuring (b) Advanced photonic processes for photovoltaics and energy storage, c) nanomaterials synthesis and diagnostics for optoelectronics and (c) biomaterials processing for tissue engineering. He has delivered more than 40 invited and keynote lectures and has been organizer and chair in major international scientific

conferences. He has over 180 SCI publications and more than 6000 citations and he has coordinated many National and EU grants. Since 2015, he is the Director of the European Nanoscience Facility of FORTH, part of the NFFA-Europe EU Infrastructure, where he is a member of the General Assembly. He is a National Representative to the High-Level Group of EU on Nanosciences, Nanotechnology and Advanced Materials and a National Expert for the Horizon 2020 committee configurations on: Nanotechnologies, Advanced materials, Biotechnology, Advanced Manufacturing and Processing. He is a member of the Scientific Committee of COST, of the Physical Sciences sectoral scientific council of the National Council for Research & Innovation of Greece and national Delegate of the OECD Working Party on Bio-, Nano- and Converging Tech (BNCT).